POLITECNICO DI TORINO
Repository ISTITUZIONALE

A comprehensive 3D fully coupled theory for thermo-magneto-electro-elastic multilayered plates and shells

Original
A comprehensive 3D fully coupled theory for thermo-magneto-electro-elastic multilayered plates and shells / Brischetto, S., Cesare, D.. - In: CURVED AND LAYERED STRUCTURES. - ISSN 2353-7396. - 13:1(2026), pp. 1-23. [10.1515/cls-2025-0052]

Availability:
This version is available at: 11583/3017254 since: 2026-10-30T18:09:22Z

Publisher:
De Gruyter Open Access

Published
DOI:10.1515/cls-2025-0052

Terms of use:

This article is made available under terms and conditions as specified in the corresponding bibliographic description in the repository

Publisher copyright

(Article begins on next page)

25 November 2026

Research Article

Salvatore Brischetto* and Domenico Cesare

A comprehensive 3D fully coupled theory for thermo-magneto-electro-elastic multilayered plates and shells

https://doi.org/10.1515/cls-2025-0052
Received June 8, 2026; accepted September 6, 2026;
published online October 30, 2026

Abstract: A three-dimensional (3D) multifield static analysis is developed for thermo-magneto-electro-elastic multilayered plates, cylinders, cylindrical shells, and spherical shells. The thermo-magneto-electro-elastic coupling is investigated through six second-order differential equations for spherical shells expressed in terms of displacements, magnetic potential, electric potential, and temperature increment. The six second-order differential equations governing spherical shells consist of the following: the 3D equilibrium equations of elasticity, the 3D divergence equation of magnetic induction, the 3D divergence equation of electric displacement, and the 3D Fourier heat-conduction equation. These equations are fully coupled and are solved in strong form by employing Navier harmonic expansions in the in-plane directions and the exponential matrix method along the thickness coordinate. The 3D thermo-magneto-electro-elastic governing equations are formulated within a mixed curvilinear orthogonal reference system, thereby enabling the analysis of spherical shells, plates, cylinders, and cylindrical panels through an appropriate selection of the two radii of curvature. The layer-wise description is implemented by enforcing interlaminar continuity conditions between adjacent layers. Such continuity conditions are imposed on displacements, magnetic potential, electric potential, temperature increments, transverse shear and normal stresses, transverse normal magnetic induction, transverse normal electric displacement, and transverse normal heat flux. The Results section presents preliminary benchmark cases in which the proposed model is assessed against other multifield formulations available in the literature for both flat and curved structures. In addition, four original case studies are introduced to investigate the fully coupled interaction among thermal, magnetic, electric, and elastic fields. These case studies consider four different geometries spanning a thickness-ratio range from thick to thin configurations. The resulting data provide insight into the influence of multifield loadings and couplings in smart structures and offer useful benchmark solutions for the verification of less refined multifield analytical and numerical 3D/2D models.

Keywords: three-dimensional formulation; multilayered shell structures; fully coupled thermo-magneto-electro-elastic behavior; layerwise approach

1 Introduction

Thermo-magneto-electro-elastic coupling represents an important research area in the field of multilayered smart structures [1, 2]. Considerable attention has recently been devoted to smart structures that can simultaneously operate as sensors and actuators [3, 4]. New materials used in these systems are continuously improving their performance and service life. For this reason, static and free vibration analyses are of fundamental importance [5, 6]. Recent studies can be classified into two main groups: free vibration and dynamic analyses, and static analyses; both categories involve thermo-magneto-electro-elastic coupling.

In the framework of free vibration studies on thermo-magneto-electro-elastic (TMEE) structures, Ansari et al. [7, 8] developed a nonlocal geometrically nonlinear beam model for TMEE nanobeams and beams; the size-dependent nonlinear forced vibration behavior was examined for different parameters. Badri Albarody and Al-Kayiem [9] modeled piezo-laminated smart shells subjected to TMEE loads. In [10], the thermo-mechanical buckling problem of functionally graded TMEE nanoplates was analyzed by imposing a Winkler–Pasternak elastic foundation under various thermal environments. Esen and Özmen [11]

***Corresponding author: Salvatore Brischetto**, Department of Mechanical and Aerospace Engineering, Politecnico di Torino, Corso Duca degli Abruzzi 24, 10129 Torino, Italy, E-mail: salvatore.brischetto@polito.it
Domenico Cesare, Department of Mechanical and Aerospace Engineering, Politecnico di Torino, Torino, Italy. https://orcid.org/0009-0008-9892-2228

Open Access. © 2026 the author(s), published by De Gruyter. This work is licensed under the Creative Commons Attribution 4.0 International License.

examined the thermal vibration and buckling behavior of functionally graded porous nanoplates embedding piezoelectric and piezomagnetic materials. The size-dependent effect in the free vibration analysis of a magneto-electro-elastic nanoshell subjected to thermo-electro-magnetic loadings was studied by Ghadiri and Safarpour [12]. Gui and Li [13] introduced a novel size-dependent model for TMEE cylindrical nanoshells made of Barium Titanate and Cobalt Ferrite materials. The buckling problem of TMEE nanocylindrical shells made of Barium Titanate and Cobalt Ferrite materials was addressed in [14]. Lang and Xuewu [15] reported the buckling and vibration analysis of functionally graded TMEE circular cylindrical shells. Li et al. [16] investigated vibration and acoustic radiation responses of TMEE functionally graded porous plates via a unified model. Liu et al. [17] proposed a size-dependent vibration model for TMEE nanobeams taking into account thermal entropy. A coupled model for forced vibrations of multi-physics composite cylindrical shells was formulated in [18] considering the improved Donnell nonlinear shell theory and Maxwell equations for electrostatics and magnetostatics. In Ni et al. [19], an analytical buckling solution, based on the Hamiltonian approach, was derived for a cylindrical shell made of two-phase TMEE composites under multi-physical fields. She and Gan [20] investigated the combined resonance in magneto-electro-elastic cylindrical shells under longitudinal and lateral excitations, and assessed the interaction between mechanical, electrical, and magnetic fields in smart structures. In Zafari et al. [21], transient TMEE coupled responses of multiferroic hybrid plates were analyzed under a distributed moving heat flux load. Shojaeefard et al. [22] investigated a rotation-induced cylindrical nano-shell (used as a water pump) subjected to electro-magnetic fields. Singh and Jaiswal [23] studied thermoelastic damping and frequency shift in thin TMEE composite nano-scale beams embedding piezoelectric and piezomagnetic materials. In [24], the nonlinear postbuckling behavior of TMEE laminated microbeams was investigated considering the modified coupled stress theory and the Reddy third-order shear deformation theory. Arefi and Zenkour [25] examined the TMEE vibration and bending behavior of multilayered/sandwich microplates and nanoplates. Mahesh et al. [26] investigated the influence of full coupling between thermal, elastic, magnetic, and electric fields on the natural frequency analysis of functionally graded TMEE plates using the finite element method. The size-dependent buckling and vibration behaviors of functionally graded TMEE Timoshenko nanobeams were discussed by Ren and Qing [27].

Thermo-Magneto-Electro-Elastic (TMEE) static analyses have been extensively investigated to understand structural behavior under multifield loadings. Aboudi [28] introduced a two-scale analysis for predicting the response of TMEE composites with localized damage subjected to remote heat flow. An analytical multiphysical response of a functionally graded thermo-magneto-elastic rotating hollow cylinder and a homogeneous orthotropic TMEE cylinder was developed by Akbarzadeh and Chen in [29]. Arefi and Zenkour [30, 31] investigated local and nonlocal TMEE bending behavior of multilayered and sandwich nanoplates. Barati and Shariyat [32] derived a fully analytical closed-form solution for functionally graded magneto-electro-hygro-thermo-elastic discs exposed to multifield loads. The three-dimensional equations of transversely isotropic TMEE materials were solved by Chen et al. [33] considering a flat crack in an infinite space subjected to symmetric mechanical, electric, magnetic, and temperature loads. Dai and Wang [34] reported an analytical solution for TMEE hollow cylinders placed in an axial magnetic field and subjected to arbitrary thermal shock, mechanical load, and transient electric excitations. The problem of an infinite multiferroic composite medium weakened by a penny-shaped crack was examined by Li et al. [35] when four pairs of generalized loads were applied on the upper and lower surfaces. A TMEE heterogeneous circular plate subjected to uniformly distributed thermal loadings was analyzed in [36]. The extended displacement discontinuity boundary integral equation was solved by Li et al. [37] for the TMEE analysis of arbitrarily shaped planar cracks in isotropic media. Serpilli [38] investigated the quasi-static behavior of a TMEE composite made of a thin plate-like layer included between two generic TMEE bodies. An analytical model for the magneto-electro-thermal bending of composite doubly-curved shallow shells reinforced by functionally graded graphene platelets was formulated by Sobhy [39]. Tong et al. [40] introduced a three-phase cylindrical model to investigate fiber composites subjected to in-plane mechanical loads under the coupling effects of thermal, electric, magnetic, and elastic fields. Tornabene et al. [41] developed an equivalent layer-wise multifield formulation involving five different physical fields (hygro-thermo-magneto-electro-elastic coupling) for laminated doubly-curved shells under thermodynamic equilibrium. Vinyas and Kattimani [42–44] examined the influence of the volume fraction of Barium-Titanate and Cobalt-Ferric oxide on the static response of multiphase magneto-electro-elastic cantilever beams and plates immersed in a thermal environment. The penny-shaped

crack problem of a TMEE infinite transversely isotropic medium subjected to a symmetric uniform heat flux was addressed by Yang et al. [45]. Zhou et al. [46] proposed an inhomogeneous magneto-electro-elastic coupling element-free Galerkin method to solve the static analysis of magneto-electro-elastic plate structures. The same authors [47] presented a cell-based smoothed finite element method coupling elastic, electric, magnetic, and thermal properties in order to characterize steady-state magneto-electro-elastic structures in a thermal environment. Zhou et al. [48] employed the TMEE enriched finite element method to analyze static models of magneto-electro-elastic smart structures. Zhang et al. [49] studied the nonlinear vibration and bending behavior of magneto-electro-elastic laminated beams in thermal environments.

The objective of the present work is to address the lack of a 3D static model for fully coupled TMEE multilayered spherical shell analyses. To this end, 3D multifield constitutive relations, 3D multifield geometrical relations, and 3D differential governing equations are formulated in terms of displacements, magnetic potential, over-temperature, and electric potential for the thermo-magneto-electro-elastic coupled problem. The 3D governing equations are expressed within a mixed curvilinear orthogonal reference system (α, β, z). The solution of the 3D multifield governing equations based on Navier harmonic forms and the exponential matrix method is discussed. Interlaminar continuity conditions between adjacent layers are imposed to introduce the layer-wise approach.

A key contribution of the present study lies in the fully thermo-magneto-electro-elastic coupling for curved structures through a 3D analytical solution in which stresses, strains, electric displacement components, magnetic induction components, and heat flux components are exactly computed. This exact methodology, capable of accurately capturing 3D effects, is extended to different geometries such as plates, cylinders, cylindrical panels, and spherical shells. This paper is part of a broader framework developed by the authors, where the 3D thermal stress analysis for multilayered and functionally graded structures was investigated in [50, 51], while static electro-elastic and static magneto-elastic coupling were thoroughly examined for both multilayered and functionally graded plates and shells in [52, 53]. More recent studies included the 3D static magneto-electro-elastic analysis of both plates [54] and shells [55]. The present contribution extends these developments by introducing, for the first time, a fully coupled four-field model (thermo-electro-magneto-elastic).

Following the review of the state of the art concerning TMEE coupling behavior in free vibration and static analyses of multilayered structures, Section 2 introduces the 3D TMEE governing equations, constitutive equations, and geometric relations; the solution methodology is also described. In Section 3, preliminary validation results and new benchmark cases are presented. The preliminary validation results are used to assess the accuracy of the proposed 3D TMEE static model for shells and plates. The new benchmark cases are included to illustrate and discuss all 3D coupling effects acting on TMEE planar and curved structures. Section 4 summarizes the main findings of the work.

2 3D thermo-magneto-electro-elastic spherical shell model

In this section, the fully coupled 3D thermo-magneto-electro-elastic spherical shell model is presented. In the first subsection, 3D thermo-magneto-electro-elastic governing equations for spherical shells are presented using the mixed curvilinear orthogonal reference system. In the second subsection, 3D geometrical relations and 3D constitutive equations for cross-ply orthotropic spherical shells are discussed. In the third subsection, the solution methodology, involving Navier harmonic forms and the exponential matrix method, is discussed in detail.

2.1 3D thermo-magneto-electro-elastic governing equations

The 3D thermo-magneto-electro-elastic governing equations for spherical shells consist of six 3D differential equations: three 3D equilibrium elastic equations (here proposed in a compact form), a 3D divergence equation for the electric displacement, a 3D divergence equation for the magnetic induction, and the 3D Fourier heat conduction equation in steady-state conditions. These six equations are written in a mixed curvilinear orthogonal reference system (α, β, z). In-plane directions α and β follow the curvature of the geometry, while the thickness direction z is rectilinear and perpendicular to the middle reference surface Ω_0. Therefore, the degeneration of the spherical shell geometry into cylinders, cylindrical shells, and plates is possible by properly considering the radii of curvature R_α and R_β. Figure 1 shows the four analyzable structures,

the mixed curvilinear orthogonal reference system, and the middle reference surface Ω_0. The six 3D equations for the thermo-magneto-electro-elastic spherical shell problem, written in the mixed curvilinear orthogonal reference system, are:

$$H_\beta \frac{\partial}{\partial \alpha}\begin{Bmatrix}\sigma^k_{\alpha\alpha}\\ \sigma^k_{\alpha\beta}\\ \sigma^k_{\alpha z}\end{Bmatrix} + H_\alpha \frac{\partial}{\partial \beta}\begin{Bmatrix}\sigma^k_{\alpha\beta}\\ \sigma^k_{\beta\beta}\\ \sigma^k_{\beta z}\end{Bmatrix} + H_\alpha H_\beta \frac{\partial}{\partial z}\begin{Bmatrix}\sigma^k_{\alpha z}\\ \sigma^k_{\beta z}\\ \sigma^k_{zz}\end{Bmatrix}$$
$$+\frac{H_\beta}{R_\alpha}\left(\begin{Bmatrix}\sigma^k_{\alpha z}\\ \sigma^k_{\beta z}\\ \sigma^k_{zz}\end{Bmatrix} - \begin{Bmatrix}-\sigma^k_{\alpha z}\\ 0\\ \sigma^k_{\alpha\alpha}\end{Bmatrix}\right) \tag{1}$$
$$+\frac{H_\alpha}{R_\beta}\left(\begin{Bmatrix}\sigma^k_{\alpha z}\\ \sigma^k_{\beta z}\\ \sigma^k_{zz}\end{Bmatrix} - \begin{Bmatrix}0\\ -\sigma^k_{\beta z}\\ \sigma^k_{\beta\beta}\end{Bmatrix}\right) = \begin{Bmatrix}0\\ 0\\ 0\end{Bmatrix},$$

$$\nabla \cdot \boldsymbol{\mathcal{D}}^k = 0, \tag{2}$$

$$\nabla \cdot \boldsymbol{\mathcal{B}}^k = 0, \tag{3}$$

$$\nabla \cdot \boldsymbol{q}^k = 0, \tag{4}$$

where σ^k_{ij} are the six stress components, $\frac{\partial}{\partial \alpha}$, $\frac{\partial}{\partial \beta}$ and $\frac{\partial}{\partial z}$ are the three partial derivatives along the three directions α, β and z, respectively. $\nabla\cdot$ indicates the divergence operator. H_α, H_β and H_z are the curvature parameters that can be written as:

$$\begin{Bmatrix}H_\alpha\\ H_\beta\\ H_z\end{Bmatrix} = \begin{Bmatrix}1+\frac{z}{R_\alpha}\\ 1+\frac{z}{R_\beta}\\ 1\end{Bmatrix} = \begin{Bmatrix}1+\frac{\tilde{z}-h/2}{R_\alpha}\\ 1+\frac{\tilde{z}-h/2}{R_\beta}\\ 1\end{Bmatrix} \tag{5}$$

$$\text{where} \quad -h/2 < z < h/2 \quad \text{and} \quad 0 < \tilde{z} < h.$$

Curvature parameters in the in-plane directions depend on the z thickness coordinate. H_z term is equal to one as no curvature is involved in the thickness direction. R_α and R_β are radii of curvature in α and β directions, respectively. The divergence operator is defined as:

$$\nabla \cdot \boldsymbol{F} = \frac{1}{H_\alpha H_\beta}\left[\frac{\partial}{\partial \alpha}(H_\beta F_\alpha) + \frac{\partial}{\partial \beta}(H_\alpha F_\beta) + \frac{\partial}{\partial z}(H_\alpha H_\beta F_z)\right], \tag{6}$$

where the vector $\boldsymbol{F} = (F_\alpha, F_\beta, F_z)$ can be $\boldsymbol{\mathcal{D}}^k$, $\boldsymbol{\mathcal{B}}^k$, or $\boldsymbol{q}^k$. $\boldsymbol{\mathcal{D}}^k = \left(\mathscr{D}^k_\alpha, \mathscr{D}^k_\beta, \mathscr{D}^k_z\right)$ is the electric displacement vector, $\boldsymbol{\mathcal{B}}^k = \left(\mathscr{B}^k_\alpha, \mathscr{B}^k_\beta, \mathscr{B}^k_z\right)$ is the magnetic induction vector, and $\boldsymbol{q}^k = \left(q^k_\alpha, q^k_\beta, q^k_z\right)$ is the heat flux vector. k indicates the generic layer in the multilayered structure. Equations (1)–(6) are obtained in accordance with [56, 57].

2.2 3D thermo-magneto-electro-elastic constitutive and geometrical equations

The 3D thermo-magneto-electro-elastic constitutive equations allow to introduce the material characteristics in the model. Stresses, electric displacement components, magnetic induction components, and heat flux components are linked to strains, electric field components, magnetic field components, and sovra-temperature. 3D thermo-magneto-electro-elastic constitutive equations can be written in matrix form for each k layer:

$$\boldsymbol{\sigma}^k = \boldsymbol{C}^k\boldsymbol{\varepsilon}^k - \boldsymbol{e}^{kT}\boldsymbol{\mathcal{E}}^k - \boldsymbol{r}^{kT}\boldsymbol{\mathcal{H}}^k - \boldsymbol{\lambda}^k\theta^k, \tag{7}$$

$$\boldsymbol{\mathcal{D}}^k = \boldsymbol{e}^k\boldsymbol{\varepsilon}^k + \boldsymbol{\epsilon}^k\boldsymbol{\mathcal{E}}^k + \boldsymbol{d}^k\boldsymbol{\mathcal{H}}^k - \boldsymbol{p}^k\theta^k, \tag{8}$$

$$\boldsymbol{\mathcal{B}}^k = \boldsymbol{r}^k\boldsymbol{\varepsilon}^k + \boldsymbol{d}^k\boldsymbol{\mathcal{E}}^k + \boldsymbol{\mu}^k\boldsymbol{\mathcal{H}}^k - \boldsymbol{g}^k\theta^k, \tag{9}$$

$$\boldsymbol{q}^k = -\boldsymbol{k}^k\nabla\theta^k, \tag{10}$$

where $\boldsymbol{\sigma}^k = \left(\sigma^k_{\alpha\alpha}, \sigma^k_{\beta\beta}, \sigma^k_{zz}, \sigma^k_{\beta z}, \sigma^k_{\alpha z}, \sigma^k_{\alpha\beta}\right)$ is the 6×1 stress vector, $\boldsymbol{\varepsilon}^k = \left(\varepsilon^k_{\alpha\alpha}, \varepsilon^k_{\beta\beta}, \varepsilon^k_{zz}, \gamma^k_{\beta z}, \gamma^k_{\alpha z}, \gamma^k_{\alpha\beta}\right)$ is the 6×1 strain vector, $\boldsymbol{\mathcal{E}}^k = \left(\mathcal{E}^k_\alpha, \mathcal{E}^k_\beta, \mathcal{E}^k_z\right)$ is the 3×1 electric field vector, $\boldsymbol{\mathcal{H}}^k = \left(\mathcal{H}^k_\alpha, \mathcal{H}^k_\beta, \mathcal{H}^k_z\right)$ is the 3×1 magnetic field vector, θ^k is the scalar over-temperature (defined as $\theta = T - T_0$, where T_0 is the reference room temperature measured in kelvin), $\boldsymbol{\mathcal{D}}^k = \left(\mathcal{D}^k_\alpha, \mathcal{D}^k_\beta, \mathcal{D}^k_z\right)$ is the 3×1 electric displacement vector, $\boldsymbol{\mathcal{B}}^k = \left(\mathcal{B}^k_\alpha, \mathcal{B}^k_\beta, \mathcal{B}^k_z\right)$ is the 3×1 magnetic induction vector, $\boldsymbol{q}^k = \left(q^k_\alpha, q^k_\beta, q^k_z\right)$ is the 3×1 heat flux vector. T means the transpose of a vector or a matrix. The gradient operator is defined as:

$$\nabla = \begin{bmatrix}\frac{1}{H_\alpha}\frac{\partial}{\partial \alpha}\\ \frac{1}{H_\beta}\frac{\partial}{\partial \beta}\\ \frac{\partial}{\partial z}\end{bmatrix}. \tag{11}$$

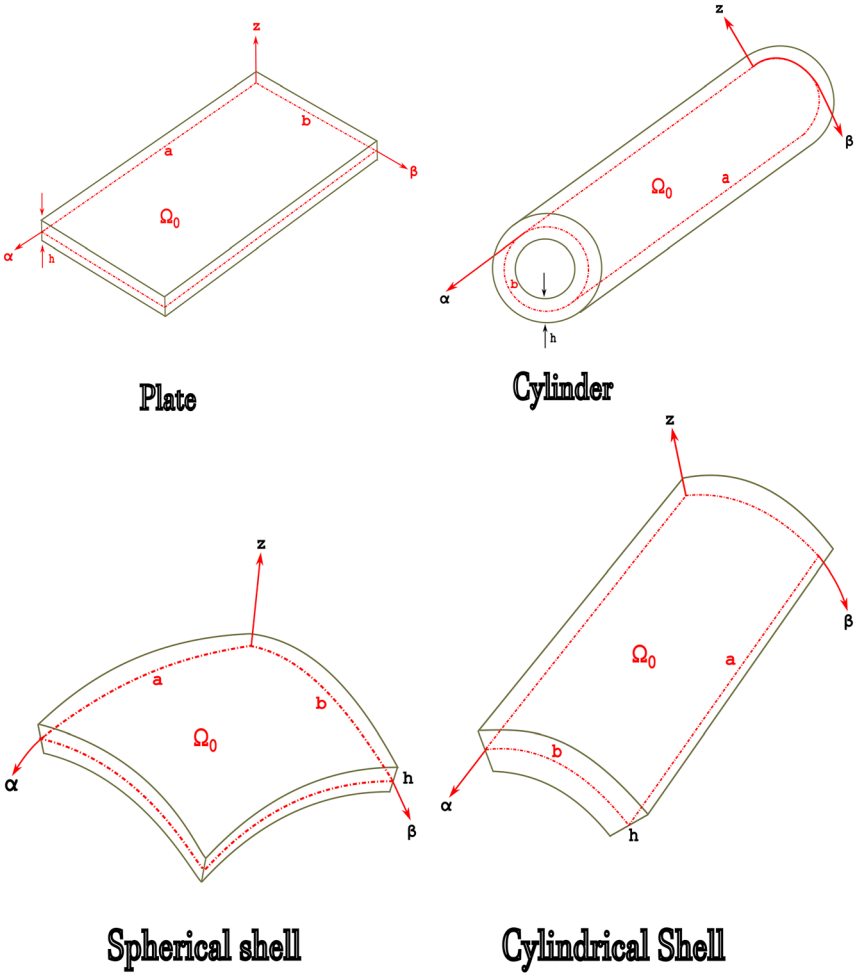

Figure 1: Geometries, mixed curvilinear orthogonal reference systems and middle reference surfaces for preliminary cases (PC) and new benchmarks (B). Dotted lines represent the middle reference surface Ω_0. The mixed curvilinear orthogonal reference system is indicated for each structure.

The proposed matrices and vectors are given in the structural reference system for each k layer for cross-ply and orthotropic materials. The 6×6 elastic coefficient matrix is:

$$\boldsymbol{C}^k = \begin{bmatrix} C_{11}^k & C_{12}^k & C_{13}^k & 0 & 0 & 0 \\ C_{12}^k & C_{22}^k & C_{23}^k & 0 & 0 & 0 \\ C_{13}^k & C_{23}^k & C_{33}^k & 0 & 0 & 0 \\ 0 & 0 & 0 & C_{44}^k & 0 & 0 \\ 0 & 0 & 0 & 0 & C_{55}^k & 0 \\ 0 & 0 & 0 & 0 & 0 & C_{66}^k \end{bmatrix}. \tag{12}$$

The 3×6 piezoelectric coefficient matrix is:

$$\boldsymbol{e}^k = \begin{bmatrix} 0 & 0 & 0 & 0 & e_{15}^k & 0 \\ 0 & 0 & 0 & e_{24}^k & 0 & 0 \\ e_{31}^k & e_{32}^k & e_{33}^k & 0 & 0 & 0 \end{bmatrix}. \tag{13}$$

The 3×6 piezoemagnetic coefficient matrix is:

$$\boldsymbol{r}^k = \begin{bmatrix} 0 & 0 & 0 & 0 & r_{15}^k & 0 \\ 0 & 0 & 0 & r_{24}^k & 0 & 0 \\ r_{31}^k & r_{32}^k & r_{33}^k & 0 & 0 & 0 \end{bmatrix}. \tag{14}$$

The 6×1 thermo-elastic coupling coefficient vector is defined as the product between the 6×6 elastic coefficient

matrix and the thermal expansion coefficients organized in an appropriate 6×1 vector:

$$\boldsymbol{\lambda}^k = \left\{ \begin{array}{c} \lambda_{11}^k \\ \lambda_{22}^k \\ \lambda_{33}^k \\ 0 \\ 0 \\ 0 \end{array} \right\} = \boldsymbol{C}^k \boldsymbol{\alpha}^k = \boldsymbol{C}^k \left\{ \begin{array}{c} \alpha_{11}^k \\ \alpha_{22}^k \\ \alpha_{33}^k \\ 0 \\ 0 \\ 0 \end{array} \right\}. \tag{15}$$

The 3×3 electric permittivity coefficient matrix is:

$$\boldsymbol{\epsilon}^k = \left[\begin{array}{ccc} \epsilon_{11}^k & 0 & 0 \\ 0 & \epsilon_{22}^k & 0 \\ 0 & 0 & \epsilon_{33}^k \end{array} \right]. \tag{16}$$

The 3×3 electro-magnetic coupling coefficient matrix is:

$$\boldsymbol{d}^k = \left[\begin{array}{ccc} d_{11}^k & 0 & 0 \\ 0 & d_{22}^k & 0 \\ 0 & 0 & d_{33}^k \end{array} \right]. \tag{17}$$

The 3×1 pyroelectric coefficient vector is:

$$\boldsymbol{p}^k = \left\{ \begin{array}{c} 0 \\ 0 \\ p_3^k \end{array} \right\}. \tag{18}$$

The 3×3 magnetic permeability coefficient matrix is:

$$\boldsymbol{\mu}^k = \left[\begin{array}{ccc} \mu_{11}^k & 0 & 0 \\ 0 & \mu_{22}^k & 0 \\ 0 & 0 & \mu_{33}^k \end{array} \right]. \tag{19}$$

The 3×1 pyromagnetic coefficient vector is:

$$\boldsymbol{g}^k = \left\{ \begin{array}{c} 0 \\ 0 \\ g_3^k \end{array} \right\}. \tag{20}$$

The 3×3 heat conduction coefficient matrix is:

$$\boldsymbol{k}^k = \left[\begin{array}{ccc} k_{11}^k & 0 & 0 \\ 0 & k_{22}^k & 0 \\ 0 & 0 & k_{33}^k \end{array} \right]. \tag{21}$$

In order to introduce the kinematic of the model, geometrical equations are requested. In this way, it is possible to link displacement vector $\boldsymbol{u}^k$, scalar electric potential ϕ^k and scalar magnetic potential ψ^k to strains, electric field and magnetic field. Geometrical equations can be written as:

$$\boldsymbol{\varepsilon}^k = \boldsymbol{\Delta}\, \boldsymbol{u}^k, \tag{22}$$

$$\boldsymbol{\mathcal{E}}^k = -\nabla \phi^k, \tag{23}$$

$$\boldsymbol{\mathcal{H}}^k = -\nabla \psi^k, \tag{24}$$

where the differential matrix $\boldsymbol{\Delta}$ and the $\boldsymbol{u}^k$ displacement vector can be defined as:

$$\boldsymbol{\Delta} = \left[\begin{array}{ccc} \frac{1}{H_\alpha}\frac{\partial}{\partial \alpha} & 0 & \frac{1}{H_\alpha R_\alpha} \\ 0 & \frac{1}{H_\beta}\frac{\partial}{\partial \beta} & \frac{1}{H_\beta R_\beta} \\ 0 & 0 & \frac{\partial}{\partial z} \\ 0 & \frac{\partial}{\partial z} - \frac{1}{H_\beta R_\beta} & \frac{1}{H_\beta}\frac{\partial}{\partial \beta} \\ \frac{\partial}{\partial z} - \frac{1}{H_\alpha R_\alpha} & 0 & \frac{1}{H_\alpha}\frac{\partial}{\partial \alpha} \\ \frac{1}{H_\beta}\frac{\partial}{\partial \beta} & \frac{1}{H_\alpha}\frac{\partial}{\partial \alpha} & 0 \end{array} \right], \tag{25}$$

$$\boldsymbol{u}^k = \left[\begin{array}{c} u^k \\ v^k \\ w^k \end{array} \right]. \tag{26}$$

2.3 Solution methodology

The substitution of Eqs. (7)–(26) into Eqs. (1)–(4) brings a set of second-order differential equations in terms of u^k, v^k, w^k, ϕ^k, ψ^k and θ^k. These are the six *primary variables* of the 3D thermo-magneto-electro-elastic problem.

The solution methodology includes the imposition of the Navier harmonic forms in the in-plane directions (α, β) for the primary variables in order to simulate the simply supported boundary conditions. The Navier harmonic forms are written as:
where $U^k(z)$, $V^k(z)$, $W^k(z)$, $\Phi^k(z)$, $\Psi^k(z)$ and $\Theta^k(z)$ are the amplitudes for each primary variable defined in appropriate

$$\begin{Bmatrix} u^k \\ v^k \\ w^k \\ \phi^k \\ \psi^k \\ \theta^k \end{Bmatrix} = \begin{bmatrix} \cos(\overline{\alpha}\alpha)\sin(\overline{\beta}\beta) & 0 & 0 & 0 & 0 & 0 \\ 0 & \sin(\overline{\alpha}\alpha)\cos(\overline{\beta}\beta) & 0 & 0 & 0 & 0 \\ 0 & 0 & \sin(\overline{\alpha}\alpha)\sin(\overline{\beta}\beta) & 0 & 0 & 0 \\ 0 & 0 & 0 & \sin(\overline{\alpha}\alpha)\sin(\overline{\beta}\beta) & 0 & 0 \\ 0 & 0 & 0 & 0 & \sin(\overline{\alpha}\alpha)\sin(\overline{\beta}\beta) & 0 \\ 0 & 0 & 0 & 0 & 0 & \sin(\overline{\alpha}\alpha)\sin(\overline{\beta}\beta) \end{bmatrix} \begin{Bmatrix} U^k(z) \\ V^k(z) \\ W^k(z) \\ \Phi^k(z) \\ \Psi^k(z) \\ \Theta^k(z) \end{Bmatrix}, \quad (27)$$

points in α–β plane where cosine and sine are simultaneously equal to 1. Terms $\overline{\alpha}$ and $\overline{\beta}$ are expressed as follows:

$$\overline{\alpha} = \frac{m\pi}{a}, \qquad \overline{\beta} = \frac{n\pi}{b}, \quad (28)$$

where m and n are the half-wave numbers and a and b indicate the in-plane dimensions of the structure in α and β directions, respectively. Thanks to the introduction of the Navier harmonic forms, the new unknowns are the amplitudes of the primary variables. Performing the derivatives of the Navier harmonic forms and introducing them in the governing equations, it is possible to write explicitly the following equations:

$$\begin{aligned}
&\left(-\frac{H_\beta C^k_{55}}{H_\alpha R^2_\alpha}-\frac{C^k_{55}}{R_\alpha R_\beta}-\overline{\alpha}^2\frac{C^k_{11}H_\beta}{H_\alpha}-\overline{\beta}^2\frac{C^k_{66}H_\alpha}{H_\beta}\right)U^k \\
&+\left(-\overline{\alpha}\overline{\beta}C^k_{12}-\overline{\alpha}\overline{\beta}C^k_{66}\right)V^k+\left(\overline{\alpha}\frac{C^k_{11}H_\beta}{H_\alpha R_\alpha}+\overline{\alpha}\frac{C^k_{12}}{R_\beta}+\overline{\alpha}\frac{C^k_{55}H_\beta}{H_\alpha R_\alpha}+\overline{\alpha}\frac{C^k_{55}}{R_\beta}\right)W^k \\
&+\left(\frac{C^k_{55}H_\beta}{R_\alpha}+\frac{C^k_{55}H_\alpha}{R_\beta}\right)U^k_{,z}+\left(\overline{\alpha}C^k_{13}H_\beta+\overline{\alpha}C^k_{55}H_\beta\right)W^k_{,z}+\left(C^k_{55}H_\alpha H_\beta\right)U^k_{,zz} \\
&+\left(+2\overline{\alpha}\frac{e^k_{15}H_\beta}{H_\alpha R_\alpha}+\overline{\alpha}\frac{e^k_{15}}{R_\beta}\right)\Phi^k+\left(\overline{\alpha}e^k_{31}H_\beta+\overline{\alpha}e^k_{15}H_\beta\right)\Phi^k_{,z} \\
&+\left(+2\overline{\alpha}\frac{r^k_{15}H_\beta}{H_\alpha R_\alpha}+\overline{\alpha}\frac{r^k_{15}}{R_\beta}\right)\Psi^k+\left(\overline{\alpha}r^k_{31}H_\beta+\overline{\alpha}r^k_{15}H_\beta\right)\Psi^k_{,z}+\left(-\overline{\alpha}\lambda^k_{11}H_\beta\right)\Theta^k=0,
\end{aligned} \quad (29)$$

$$\begin{aligned}
&\left(-\frac{H_\alpha C^k_{44}}{H_\beta R^2_\beta}-\frac{C^k_{44}}{R_\alpha R_\beta}-\overline{\alpha}^2\frac{C^k_{66}H_\beta}{H_\alpha}-\overline{\beta}^2\frac{C^k_{22}H_\alpha}{H_\beta}\right)V^k \\
&+\left(-\overline{\alpha}\overline{\beta}C^k_{12}-\overline{\alpha}\overline{\beta}C^k_{66}\right)U^k+\left(\overline{\beta}\frac{C^k_{44}H_\alpha}{H_\beta R_\beta}+\overline{\beta}\frac{C^k_{44}}{R_\alpha}+\overline{\beta}\frac{C^k_{22}H_\alpha}{H_\beta R_\beta}+\overline{\beta}\frac{C^k_{12}}{R_\alpha}\right)W^k \\
&+\left(\frac{C^k_{44}H_\alpha}{R_\beta}+\frac{C^k_{44}H_\beta}{R_\alpha}\right)V^k_{,z}+\left(\overline{\beta}C^k_{44}H_\alpha+\overline{\beta}C^k_{23}H_\alpha\right)W^k_{,z}+\left(C^k_{44}H_\alpha H_\beta\right)V^k_{,zz} \\
&+\left(+2\overline{\beta}\frac{e^k_{24}H_\alpha}{H_\beta R_\beta}+\overline{\beta}\frac{e^k_{24}}{R_\alpha}\right)\Phi^k+\left(\overline{\beta}e^k_{32}H_\alpha+\overline{\beta}e^k_{24}H_\alpha\right)\Phi^k_{,z} \\
&+\left(+2\overline{\beta}\frac{r^k_{24}H_\alpha}{H_\beta R_\beta}+\overline{\beta}\frac{r^k_{24}}{R_\alpha}\right)\Psi^k+\left(\overline{\beta}r^k_{32}H_\alpha+\overline{\beta}r^k_{24}H_\alpha\right)\Psi^k_{,z}+\left(-\overline{\beta}\lambda^k_{22}H_\alpha\right)\Theta^k=0,
\end{aligned} \quad (30)$$

$$\begin{aligned}
&\left(\frac{C^k_{13}}{R_\alpha R_\beta}+\frac{C^k_{23}}{R_\alpha R_\beta}-\frac{C^k_{11}H_\beta}{H_\alpha R^2_\alpha}-\frac{2C^k_{12}}{R_\alpha R_\beta}-\frac{C^k_{22}H_\alpha}{H_\beta R^2_\beta}-\overline{\alpha}^2\frac{C^k_{55}H_\beta}{H_\alpha}-\overline{\beta}^2\frac{C^k_{44}H_\alpha}{H_\beta}\right)W^k \\
&+\left(\overline{\alpha}\frac{C^k_{55}H_\beta}{H_\alpha R_\alpha}-\overline{\alpha}\frac{C^k_{13}}{R_\beta}+\overline{\alpha}\frac{C^k_{11}H_\beta}{H_\alpha R_\alpha}+\overline{\alpha}\frac{C^k_{12}}{R_\beta}\right)U^k \\
&+\left(\overline{\beta}\frac{C^k_{44}H_\alpha}{H_\beta R_\beta}-\overline{\beta}\frac{C^k_{23}}{R_\alpha}+\overline{\beta}\frac{C^k_{22}H_\alpha}{H_\beta R_\beta}+\overline{\beta}\frac{C^k_{12}}{R_\alpha}\right)V^k \\
&+\left(-\overline{\alpha}C^k_{55}H_\beta-\overline{\alpha}C^k_{13}H_\beta\right)U^k_{,z}+\left(-\overline{\beta}C^k_{44}H_\alpha-\overline{\beta}C^k_{23}H_\alpha\right)V^k_{,z} \\
&+\left(\frac{C^k_{33}H_\beta}{R_\alpha}+\frac{C^k_{33}H_\alpha}{R_\beta}\right)W^k_{,z} \\
&+\left(C^k_{33}H_\alpha H_\beta\right)W^k_{,zz}+\left(-\overline{\alpha}^2\frac{e^k_{15}H_\beta}{H_\alpha}-\overline{\beta}^2\frac{e^k_{24}H_\alpha}{H_\beta}\right)\Phi^k \\
&+\left(-\overline{\alpha}^2\frac{r^k_{15}H_\beta}{H_\alpha}-\overline{\beta}^2\frac{r^k_{24}H_\alpha}{H_\beta}\right)\Psi^k \\
&+\left(-\frac{e^k_{31}H_\beta}{R_\alpha}-\frac{e^k_{32}H_\alpha}{R_\beta}+\frac{e^k_{33}H_\beta}{R_\alpha}+\frac{e^k_{33}H_\alpha}{R_\beta}\right)\Phi^k_{,z}+\left(e^k_{33}H_\alpha H_\beta\right)\Phi^k_{,zz} \\
&+\left(-\frac{r^k_{31}H_\beta}{R_\alpha}-\frac{r^k_{32}H_\alpha}{R_\beta}+\frac{r^k_{33}H_\beta}{R_\alpha}+\frac{r^k_{33}H_\alpha}{R_\beta}\right)\Psi^k_{,z}+\left(r^k_{33}H_\alpha H_\beta\right)\Psi^k_{,zz} \\
&+\left(\frac{\lambda^k_{11}H_\beta}{R_\alpha}+\frac{\lambda^k_{22}H_\alpha}{R_\beta}-\frac{\lambda^k_{33}H_\beta}{R_\alpha}-\frac{\lambda^k_{33}H_\alpha}{R_\beta}\right)\Theta^k+\left(-\lambda_{33}H_\alpha H_\beta\right)\Theta^k_{,z}=0,
\end{aligned} \quad (31)$$

$$\begin{aligned}
&\left(\overline{\alpha}\frac{e^k_{15}}{H^2_\alpha R_\alpha}\right)U^k+\left(\overline{\beta}\frac{e^k_{24}}{H^2_\beta R_\beta}\right)V^k+\left(-\overline{\alpha}^2\frac{e^k_{15}}{H^2_\alpha}-\overline{\beta}^2\frac{e^k_{24}}{H^2_\beta}\right)W^k \\
&+\left(-\overline{\alpha}\frac{e^k_{15}}{H_\alpha}-\overline{\alpha}\frac{e^k_{31}}{H_\alpha}\right)U^k_{,z}+\left(-\overline{\beta}\frac{e^k_{24}}{H_\beta}-\overline{\beta}\frac{e^k_{32}}{H_\beta}\right)V^k_{,z} \\
&+\left(\frac{e^k_{31}}{H_\alpha R_\alpha}+\frac{e^k_{32}}{H_\beta R_\beta}\right)W^k_{,z}+\left(e^k_{33}\right)W^k_{,zz}+\left(\overline{\alpha}^2\frac{\epsilon^k_{11}}{H^2_\alpha}+\overline{\beta}^2\frac{\epsilon^k_{22}}{H^2_\beta}\right)\Phi^k \\
&+\left(-e^k_{33}\right)\Phi^k_{,zz}+\left(\overline{\alpha}^2\frac{d^k_{11}}{H^2_\alpha}+\overline{\beta}^2\frac{d^k_{22}}{H^2_\beta}\right)\Psi^k+\left(-d^k_{33}\right)\Psi^k_{,zz} \\
&+\left(p^k_3\right)\Theta^k_{,z}=0,
\end{aligned} \quad (32)$$

$$\left(\overline{\alpha}\frac{r^k_{15}}{H^2_\alpha R_\alpha}\right)U^k+\left(\overline{\beta}\frac{r^k_{24}}{H^2_\beta R_\beta}\right)V^k+\left(-\overline{\alpha}^2\frac{r^k_{15}}{H^2_\alpha}-\overline{\beta}^2\frac{r^k_{24}}{H^2_\beta}\right)W^k$$
$$+\left(-\overline{\alpha}\frac{r^k_{15}}{H_\alpha}-\overline{\alpha}\frac{r^k_{31}}{H_\alpha}\right)U^k_{,z}+\left(-\overline{\beta}\frac{r^k_{24}}{H_\beta}-\overline{\beta}\frac{r^k_{32}}{H_\beta}\right)V^k_{,z}$$
$$+\left(\frac{r^k_{31}}{H_\alpha R_\alpha}+\frac{r^k_{32}}{H_\beta R_\beta}\right)W^k_{,z}+\left(\overline{\alpha}^2\frac{d^k_{11}}{H^2_\alpha}+\overline{\beta}^2\frac{d^k_{22}}{H^2_\beta}\right)\Phi^k+\left(-d^k_{33}\right)\Phi^k_{,zz} \tag{33}$$
$$+\left(\overline{\alpha}^2\frac{\mu^k_{11}}{H^2_\alpha}+\overline{\beta}^2\frac{\mu^k_{22}}{H^2_\beta}\right)\Psi^k+(-\mu^k_{33})\Psi^k_{,zz}+(g^k_3)\Theta^k_{,z}=0,$$

$$\left(-\overline{\alpha}^2\frac{k^k_{11}}{H^2_\alpha}-\overline{\beta}^2\frac{k^k_{22}}{H^2_\beta}\right)\Theta^k+\left(k^k_{33}\right)\Theta^k_{,zz}=0. \tag{34}$$

A compact form of Eqs. (29)–(34) is possible by renaming the terms in round brackets:

$$A^k_1U^k+A^k_2V^k+A^k_3W^k+A^k_4\Phi^k+A^k_5\Psi^k+J^k_1\Theta^k+A^k_6U^k_{,z}$$
$$+A^k_7W^k_{,z}+A^k_8\Phi^k_{,z}+A^k_9\Psi^k_{,z}+A^k_{10}U^k_{,zz}=0, \tag{35}$$

$$A^k_{11}U^k+A^k_{12}V^k+A^k_{13}W^k+A^k_{14}\Phi^k+A^k_{15}\Psi^k+J^k_2\Theta^k+A^k_{16}V^k_{,z}$$
$$+A^k_{17}W^k_{,z}+A^k_{18}\Phi^k_{,z}+A^k_{19}\Psi^k_{,z}+A^k_{20}V^k_{,zz}=0, \tag{36}$$

$$A^k_{21}U^k+A^k_{22}V^k+A^k_{23}W^k+A^k_{24}\Phi^k+A^k_{25}\Psi^k+J^k_3\Theta^k+A^k_{26}U^k_{,z}$$
$$+A^k_{27}V^k_{,z}+A^k_{28}W^k_{,z}+A^k_{29}\Phi^k_{,z}+A^k_{30}\Psi^k_{,z}+J^k_4\Theta^k_{,z}+A^k_{31}W^k_{,zz} \tag{37}$$
$$+A^k_{32}\Phi^k_{,zz}+A^k_{33}\Psi^k_{,zz}=0,$$

$$A^k_{34}U^k+A^k_{35}V^k+A^k_{36}W^k+A^k_{37}\Phi^k+A^k_{38}\Psi^k+A^k_{39}U^k_{,z}+A^k_{40}V^k_{,z}$$
$$+A^k_{41}W^k_{,z}+J^k_5\Theta^k_{,z}+A^k_{42}W^k_{,zz}+A^k_{43}\Phi^k_{,zz}+A^k_{44}\Psi^k_{,zz}=0, \tag{38}$$

$$A^k_{45}U^k+A^k_{46}V^k+A^k_{47}W^k+A^k_{48}\Phi^k+A^k_{49}\Psi^k+A^k_{50}U^k_{,z}+A^k_{51}V^k_{,z}$$
$$+A^k_{52}W^k_{,z}+J^k_6\Theta^k_{,z}+A^k_{53}W^k_{,zz}+A^k_{54}\Phi^k_{,zz}+A^k_{55}\Psi^k_{,zz}=0. \tag{39}$$

$$J^k_7\Theta^k+J^k_8\Theta^k_{,zz}=0. \tag{40}$$

Equations (35)–(40) are a set of six second order differential equations in z. In order to solve this set of equations with the exponential matrix method, constant coefficients and first-order differential equations must be obtained. A^k_i and J^k_i coefficients become constant for very thin mathematical layers introduced in the thickness direction z. In this way, curvature terms H_α and H_β lose their dependence from z. In fact, value z does not vary within each thin mathematical layer. Thanks to this approach, A^j_i and J^j_i can be considered as constant coefficients because all equations and related terms are written for a general j thin mathematical layer. M will be defined as the total number of mathematical layers. In order to have first-order differential equations, redoubling primary variable procedure for second-order differential equations is adopted. In this way, Eqs. (35)–(40) can be rewritten in matrix form as follows:

$$\boldsymbol{D}^j\boldsymbol{X}^j_{,z}=\boldsymbol{A}^j\boldsymbol{X}^j \qquad \Rightarrow \qquad \boldsymbol{X}^j_{,z}=\boldsymbol{A}^{*j}\boldsymbol{X}^j \tag{41}$$

where $\boldsymbol{X}^j$ is the 12×1 vector of unknowns, $\boldsymbol{X}^j_{,z}$ is the 12×1 vector of unknowns derived with respect to z, $\boldsymbol{D}^j$ and $\boldsymbol{A}^j$ are the 12×12 coefficient matrices and $\boldsymbol{A}^{*j}$ is the 12×12 coefficient matrix computed as $\boldsymbol{A}^{*j}=\boldsymbol{D}^{j-1}\boldsymbol{A}^j$. Vectors $\boldsymbol{X}^j$, $\boldsymbol{X}^j_{,z}$ and matrices $\boldsymbol{D}^j$, $\boldsymbol{A}^j$ can be explicitly written as:

$$\boldsymbol{X}^j=\left\{\begin{matrix}U\\V\\W\\\Phi\\\Psi\\\Theta\\U_{,z}\\V_{,z}\\W_{,z}\\\Phi_{,z}\\\Psi_{,z}\\\Theta_{,z}\end{matrix}\right\}^j, \tag{42}$$

$$\boldsymbol{X}^j_{,z}=\left\{\begin{matrix}U\\V\\W\\\Phi\\\Psi\\\Theta\\U_{,z}\\V_{,z}\\W_{,z}\\\Phi_{,z}\\\Psi_{,z}\\\Theta_{,z}\end{matrix}\right\}^j_{,z}, \tag{43}$$

$$\boldsymbol{D}^j=\begin{bmatrix}A_{10}&0&0&0&0&0&0&0&0&0&0&0\\0&A_{20}&0&0&0&0&0&0&0&0&0&0\\0&0&P_1&0&0&0&0&0&0&0&0&0\\0&0&0&P_1&0&0&0&0&0&0&0&0\\0&0&0&0&P_1&0&0&0&0&0&0&0\\0&0&0&0&0&J_8&0&0&0&0&0&0\\0&0&0&0&0&0&A_{10}&0&0&0&0&0\\0&0&0&0&0&0&0&A_{20}&0&0&0&0\\0&0&0&0&0&0&0&0&P_1&0&0&0\\0&0&0&0&0&0&0&0&0&P_1&0&0\\0&0&0&0&0&0&0&0&0&0&P_1&0\\0&0&0&0&0&0&0&0&0&0&0&J_8\end{bmatrix}^j, \tag{44}$$

$$\boldsymbol{A}^j = \begin{bmatrix} 0 & 0 & 0 & 0 & 0 & 0 & A_{10} & 0 & 0 & 0 & 0 & 0 \\ 0 & 0 & 0 & 0 & 0 & 0 & 0 & A_{20} & 0 & 0 & 0 & 0 \\ 0 & 0 & 0 & 0 & 0 & 0 & 0 & 0 & P_1 & 0 & 0 & 0 \\ 0 & 0 & 0 & 0 & 0 & 0 & 0 & 0 & 0 & P_1 & 0 & 0 \\ 0 & 0 & 0 & 0 & 0 & 0 & 0 & 0 & 0 & 0 & P_1 & 0 \\ 0 & 0 & 0 & 0 & 0 & 0 & 0 & 0 & 0 & 0 & 0 & J_8 \\ -A_1 & -A_2 & -A_3 & -A_4 & -A_5 & -J_1 & -A_6 & 0 & -A_7 & -A_8 & -A_9 & 0 \\ -A_{11} & -A_{12} & -A_{13} & -A_{14} & -A_{15} & -J_2 & 0 & -A_{16} & -A_{17} & -A_{18} & -A_{19} & 0 \\ -P_2 & -P_3 & -P_4 & -P_5 & -P_6 & -R_1 & -P_7 & -P_8 & -P_9 & -P_{10} & -P_{11} & -R_2 \\ -P_{12} & -P_{13} & -P_{14} & -P_{15} & -P_{16} & -R_3 & -P_{17} & -P_{18} & -P_{19} & -P_{20} & -P_{21} & -R_4 \\ -P_{22} & -P_{23} & -P_{24} & -P_{25} & -P_{26} & -R_5 & -P_{27} & -P_{28} & -P_{29} & -P_{30} & -P_{31} & -R_6 \\ 0 & 0 & 0 & 0 & 0 & -J_7 & 0 & 0 & 0 & 0 & 0 & 0 \end{bmatrix}^j. \tag{45}$$

twhere P_i^j terms are combinations of A_i^j terms; R_i^j terms are combinations of A_i^j and J_i^j terms. A solution of Eq. (41) can be obtained using the exponential matrix method:

$$\boldsymbol{X}^j(h_j) = \exp\left(\boldsymbol{A}^{*j} h_j\right) \boldsymbol{X}^j(0) = \left[\sum_{i=0}^{N} \frac{(\boldsymbol{A}^{*j})^i}{i!} h_j^i\right] \boldsymbol{X}^j(0), \tag{46}$$

where $(\boldsymbol{A}^{*j})^0 = \boldsymbol{I}$ is the 12×12 identity matrix. $\tilde{z}_j = h_j$ is the top of the j layer and $\tilde{z}_j = 0$ is the bottom of the j layer.

The layer wise approach is introduced thanks to congruence and equilibrium conditions between two contiguous j mathematical layers: they are also called interlaminar continuity conditions. Interlaminar continuity conditions are written as follows:

$$u_b^j = u_t^{j-1}, \quad v_b^j = v_t^{j-1}, \quad w_b^j = w_t^{j-1}, \quad \phi_b^j = \phi_t^{j-1}, \quad \psi_b^j = \psi_t^{j-1}, \quad \theta_b^j = \theta_t^{j-1}, \tag{47}$$

$$\sigma_{\alpha z_b}^j = \sigma_{\alpha z_t}^{j-1}, \quad \sigma_{\beta z_b}^j = \sigma_{\beta z_t}^{j-1}, \quad \sigma_{z z_b}^j = \sigma_{z z_t}^{j-1}, \quad \mathscr{D}_{z_b}^j = \mathscr{D}_{z_t}^{j-1}, \quad \mathscr{B}_{z_b}^j = \mathscr{B}_{z_t}^{j-1}, \quad q_{z_b}^j = q_{z_t}^{j-1}, \tag{48}$$

t is the top of the previous $j-1$ layer and b is the bottom of the next j layer.

By introducing Eqs. (7)–(27) into Eqs. (47) and (48), interlaminar continuity conditions can be written explicitly in terms of maximum amplitudes:

$$U_b^j = U_t^{j-1}, \tag{49}$$

$$V_b^j = V_t^{j-1}, \tag{50}$$

$$W_b^j = W_t^{j-1}, \tag{51}$$

$$\Phi_b^j = \Phi_t^{j-1}, \tag{52}$$

$$\Psi_b^j = \Psi_t^{j-1}, \tag{53}$$

$$\Theta_b^j = \Theta_t^{j-1}, \tag{54}$$

$$\frac{C_{55}^j}{H_{\alpha_b}^j}\bar{\alpha} W_b^j + C_{55}^j U_{,z_b}^j - \frac{C_{55}^j}{H_{\alpha_b}^j R_\alpha} U_b^j + \frac{e_{15}^j}{H_{\alpha_b}^j}\bar{\alpha}\Phi_b^j + \frac{r_{15}^j}{H_{\alpha_b}^j}\bar{\alpha}\Psi_b^j = + \frac{C_{55}^{j-1}}{H_{\alpha_t}^{j-1}}\bar{\alpha} W_t^{j-1} + C_{55}^{j-1} U_{,z_t}^{j-1} - \frac{C_{55}^{j-1}}{H_{\alpha_t}^{j-1} R_\alpha} U_t^{j-1} + \frac{e_{15}^{j-1}}{H_{\alpha_t}^{j-1}}\bar{\alpha}\Phi_t^{j-1} + \frac{r_{15}^{j-1}}{H_{\alpha_t}^{j-1}}\bar{\alpha}\Psi_t^{j-1}, \tag{55}$$

$$\frac{C_{44}^j}{H_{\beta_b}^j}\bar{\beta} W_b^j + C_{44}^j V_{,z_b}^j - \frac{C_{44}^j}{H_{\beta_b}^j R_\beta} V_b^j + \frac{e_{24}^j}{H_{\beta_b}^j}\bar{\beta}\Phi_b^j + \frac{r_{24}^j}{H_{\beta_b}^j}\bar{\beta}\Psi_b^j = + \frac{C_{44}^{j-1}}{H_{\beta_t}^{j-1}}\bar{\beta} W_t^{j-1} + C_{44}^{j-1} V_{,z_t}^{j-1} - \frac{C_{44}^{j-1}}{H_{\beta_t}^{j-1} R_\beta} V_t^{j-1} + \frac{e_{24}^{j-1}}{H_{\beta_t}^{j-1}}\bar{\beta}\Phi_t^{j-1} + \frac{r_{24}^{j-1}}{H_{\beta_t}^{j-1}}\bar{\beta}\Psi_t^{j-1}, \tag{56}$$

$$\begin{aligned} &-\frac{C_{13}^j}{H_{\alpha_b}^j}\bar{\alpha} U_b^j + \frac{C_{13}^j}{H_{\alpha_b}^j R_\alpha} W_b^j - \frac{C_{23}^j}{H_{\beta_b}^j}\bar{\beta} V_b^j + \frac{C_{23}^j}{H_{\beta_b}^j R_\beta} W_b^j \\ &-\lambda_{33}^j \Theta_b^j + C_{33}^j W_{,z_b}^j + e_{33}^j \Phi_{,z_b}^j + r_{33}^j \Psi_{,z_b}^j = -\frac{C_{13}^{j-1}}{H_{\alpha_t}^{j-1}}\bar{\alpha} U_t^{j-1} \\ &+\frac{C_{13}^{j-1}}{H_{\alpha_t}^{j-1} R_\alpha} W_t^{j-1} - \frac{C_{23}^{j-1}}{H_{\beta_t}^{j-1}}\bar{\beta} V_t^{j-1} + \frac{C_{23}^{j-1}}{H_{\beta_t}^{j-1} R_\beta} W_t^{j-1} \\ &-\lambda_{33}^{j-1} \Theta_t^{j-1} + C_{33}^{j-1} W_{,z_t}^{j-1} + e_{33}^{j-1} \Phi_{,z_t}^{j-1} + r_{33}^{j-1} \Psi_{,z_t}^{j-1}, \end{aligned} \tag{57}$$

$$\begin{aligned} &-\frac{e_{31}^j}{H_{\alpha_b}^j}\bar{\alpha} U_b^j + \frac{e_{31}^j}{H_{\alpha_b}^j R_\alpha} W_b^j - \frac{e_{32}^j}{H_{\beta_b}^j}\bar{\beta} V_b^j \\ &+\frac{e_{32}^j}{H_{\beta_b}^j R_\beta} W_b^j + p_3^j \Theta_b^j + e_{33}^j W_{,z_b}^j - \epsilon_{33}^j \Phi_{,z_b}^j - d_{33}^j \Psi_{,z_b}^j \\ &= -\frac{e_{31}^{j-1}}{H_{\alpha_t}^{j-1}}\bar{\alpha} U_t^j + \frac{e_{31}^{j-1}}{H_{\alpha_t}^{j-1} R_\alpha} W_t^j - \frac{e_{32}^{j-1}}{H_{\beta_t}^{j-1}}\bar{\beta} V_t^j \\ &+\frac{e_{32}^{j-1}}{H_{\beta_t}^{j-1} R_\beta} W_t^j + p_3^{j-1} \Theta_t^{j-1} + + e_{33}^{j-1} W_{,z_t}^{j-1} - \epsilon_{33}^{j-1} \Phi_{,z_t}^{j-1} - d_{33}^{j-1} \Psi_{,z_t}^{j-1}, \end{aligned} \tag{58}$$

$$
\begin{aligned}
&-\frac{r^j_{31}}{H^j_{\alpha_b}}\overline{\alpha}U^j_b+\frac{r^j_{31}}{H^j_{\alpha_b}R_\alpha}W^j_b-\frac{r^j_{32}}{H^j_{\beta_b}}\overline{\beta}V^j_b\\
&+\frac{r^j_{32}}{H^j_{\beta_b}R_\beta}W^j_b+g^j_3\Theta^j_b+r^j_{33}W^j_{,z_b}-d^j_{33}\Phi^j_{,z_b}-\mu^j_{33}\Psi^j_{,z_b}\\
&=-\frac{r^{j-1}_{31}}{H^{j-1}_{\alpha_t}}\overline{\alpha}U^j_t+\frac{r^{j-1}_{31}}{H^{j-1}_{\alpha_t}R_\alpha}W^j_t-\frac{r^{j-1}_{32}}{H^{j-1}_{\beta_t}}\overline{\beta}V^j_t\\
&+\frac{r^{j-1}_{32}}{H^{j-1}_{\beta_t}R_\beta}W^j_t+g^{j-1}_3\Theta^{j-1}_t+q^{j-1}_{33}W^{j-1}_{,z_t}-d^{j-1}_{33}\Phi^{j-1}_{,z_t}-\mu^{j-1}_{33}\Phi^{j-1}_{,z_t},
\end{aligned}
\tag{59}
$$

$$
-k^j_{33}\Theta^j_{,z_b}=-k^{j-1}_{33}\Theta^{j-1}_{,z_t}. \tag{60}
$$

Equations (49)–(60) can be compacted in a matrix form as follows:

$$
\boldsymbol{X}^j(0)=\boldsymbol{T}^{j,j-1}\boldsymbol{X}^{j-1}(h_{j-1}), \tag{61}
$$

where $\boldsymbol{T}^{j,j-1}$ is the 12×12 *transfer matrix* linking the bottom $(\tilde{z}_j=0)$ of the j layer and the top $(\tilde{z}_{j-1}=h_{j-1})$ of the $j-1$ layer. Matrix $\boldsymbol{T}^{j,j-1}$ can be explicitly written as:

$$
\boldsymbol{T}^{j,j-1}=\begin{bmatrix}
1 & 0 & 0 & 0 & 0 & 0 & 0 & 0 & 0 & 0 & 0 & 0\\
0 & 1 & 0 & 0 & 0 & 0 & 0 & 0 & 0 & 0 & 0 & 0\\
0 & 0 & 1 & 0 & 0 & 0 & 0 & 0 & 0 & 0 & 0 & 0\\
0 & 0 & 0 & 1 & 0 & 0 & 0 & 0 & 0 & 0 & 0 & 0\\
0 & 0 & 0 & 0 & 1 & 0 & 0 & 0 & 0 & 0 & 0 & 0\\
0 & 0 & 0 & 0 & 0 & 1 & 0 & 0 & 0 & 0 & 0 & 0\\
T_1 & 0 & T_2 & T_3 & T_4 & 0 & T_5 & 0 & 0 & 0 & 0 & 0\\
0 & T_6 & T_7 & T_8 & T_9 & 0 & 0 & T_{10} & 0 & 0 & 0 & 0\\
T_{11} & T_{12} & T_{13} & 0 & 0 & \tau_1 & 0 & 0 & T_{14} & T_{15} & T_{16} & 0\\
T_{17} & T_{18} & T_{19} & 0 & 0 & \tau_2 & 0 & 0 & T_{20} & T_{21} & T_{22} & 0\\
T_{23} & T_{24} & T_{25} & 0 & 0 & \tau_3 & 0 & 0 & T_{26} & T_{27} & T_{28} & 0\\
0 & 0 & 0 & 0 & 0 & 0 & 0 & 0 & 0 & 0 & 0 & \tau_4
\end{bmatrix}^{j,j-1}. \tag{62}
$$

By considering a recursive combination of Eqs. (46)–(62), it is possible to link the bottom $(\tilde{z}_1=0)$ of the first (1) layer with the top $(\tilde{z}_M=h_M)$ of the last (M) one. The resulting equation takes the following form:

$$
\begin{aligned}
\boldsymbol{X}^M(h_M)&=\boldsymbol{A}^{**M}\boldsymbol{T}^{M,M-1}\boldsymbol{A}^{**M-1}\ldots\boldsymbol{T}^{2,1}\boldsymbol{A}^{**1}\boldsymbol{X}^1(0)\\
&=\boldsymbol{H_m}\boldsymbol{X}^1(0).
\end{aligned}
\tag{63}
$$

Matrix $\boldsymbol{H_m}$ is the *multilayered* matrix that includes all the multilayer structure peculiarities (in-plane dimensions, thickness, material layer configuration, interlaminar continuity conditions). Independently of the order N of the exponential matrix and the total number M of mathematical layers used for the multilayer configuration, $\boldsymbol{H_m}$ is always a 12×12 matrix. This approach enables very fast computation even if a layer wise approach is adopted.

Boundary constraints are the simply-supported ones as they are naturally fulfilled at the edges by Eq. (27). Simply-supported constraints can be written as follows:

$$
\begin{aligned}
&v^k=0,\ w^k=0,\ \phi^k=0,\ \psi^k=0,\ \theta^k=0,\ \sigma^k_{\alpha\alpha}=0 \quad \text{for} \quad \alpha=0,a,\\
&u^k=0,\ w^k=0,\ \phi^k=0,\ \psi^k=0,\ \theta^k=0,\ \sigma^k_{\beta\beta}=0 \quad \text{for} \quad \beta=0,b.
\end{aligned}
\tag{64}
$$

Load boundary conditions must be imposed at the outer surfaces of the structure. Load boundary conditions involve a combination of elastic, magnetic, electric, and thermal fields in terms of pressure load, magnetic potential or transverse normal magnetic induction, electric potential or transverse normal electric induction, and over-temperature. For the elastic field, load boundary conditions can be imposed as:

$$
\sigma_{zz}=\overline{P}_z(z)\sin(\overline{\alpha}\alpha)\sin(\overline{\beta}\beta) \quad \text{for} \quad \tilde{z}=0,h, \tag{65}
$$

For the magnetic field, load boundary conditions can be written as:

$$
\begin{aligned}
\psi&=\overline{\Psi}(z)\sin(\overline{\alpha}\alpha)\sin(\overline{\beta}\beta) \qquad \text{or} \qquad \mathcal{B}_z\\
&=\overline{\mathcal{B}}_z(z)\sin(\overline{\alpha}\alpha)\sin(\overline{\beta}\beta) \qquad \text{for} \quad \tilde{z}=0,h,
\end{aligned}
\tag{66}
$$

Load boundary conditions for the electric field can be written as:

$$
\begin{aligned}
\phi&=\overline{\Phi}(z)\sin(\overline{\alpha}\alpha)\sin(\overline{\beta}\beta) \qquad \text{or} \qquad \mathcal{D}_z\\
&=\overline{\mathcal{D}}_z(z)\sin(\overline{\alpha}\alpha)\sin(\overline{\beta}\beta) \qquad \text{for} \quad \tilde{z}=0,h,
\end{aligned}
\tag{67}
$$

Load boundary conditions in terms of over-temperature can be written as follows:

$$\theta = \overline{\Theta}(z)\sin(\overline{\alpha}\alpha)\sin(\overline{\beta}\beta) \qquad \text{for} \quad \widetilde{z} = 0, h, \tag{68}$$

The overbar added on the amplitude terms means imposed values. All the possible combinations of these four load boundary conditions can be written in a general matrix form as:

$$\boldsymbol{B}_b^1 \boldsymbol{X}^1(0) = \boldsymbol{P}_b, \tag{69}$$

$$\boldsymbol{B}_t^M \boldsymbol{X}^M(h_M) = \boldsymbol{P}_t, \tag{70}$$

where $\boldsymbol{B}_b^1$ and $\boldsymbol{B}_t^M$ are the 6×12 multifield load boundary condition matrices defined at the bottom (b) of the first layer (1) and at the top (t) of the last layer (M). $\boldsymbol{P}_b$ and $\boldsymbol{P}_t$ are the 6×1 multifield load vectors at the bottom (b) and at the top (t) of the shell. Taking into account Eq. (63), it is possible to rewrite Eqs. (69) and (70) as:

$$\begin{bmatrix} \boldsymbol{B}_b^1 \\ \boldsymbol{B}_t^M \boldsymbol{H}_{\boldsymbol{m}} \end{bmatrix} \boldsymbol{X}_b^1 = \begin{Bmatrix} \boldsymbol{P}_{\boldsymbol{b}} \\ \boldsymbol{P}_{\boldsymbol{t}} \end{Bmatrix} \qquad \Rightarrow \qquad \boldsymbol{E}\boldsymbol{X}_b^1 = \boldsymbol{P}. \tag{71}$$

$\boldsymbol{X}_b^1 = \boldsymbol{X}^1(0)$ is the unknown vector at the bottom (b) of the first (1) layer. $\boldsymbol{E}$ is the 12×12 matrix including all the characteristics of the multilayered configuration. Solving the linear system in Eq. (71), the exact 3D solution at the bottom of the structure is obtained. Thanks to the recursively use of Eqs. (46)–(63), the amplitudes of the primary variables along the entire thickness direction can be evaluated. After the primary variable reconstructions along the thickness direction, the other variables can be obtained by using Eqs. (7)–(10).

The present formulation has been implemented using the MATLAB environment and developing an in-house academic code called *3D Exponential Multifield Solutions (3DEMS)*.

3 Results

In this section, results obtained with the present 3D thermo-magneto-electro-elastic shell model are shown. Results referring to the 3D model shown in Section 2 will be indicated with the acronym 3D–u–θ–ϕ–ψ. This acronym is useful to recognize the main peculiarities of the model: a three-dimensional model (3D) where displacements (u), over-temperature (θ), electric potential (ϕ) and magnetic potential (ψ) are the primary variables. In the preliminary case subsection, comparisons are proposed between 3D three-field models from the open literature and the present 3D–u–θ–ϕ–ψ model. In the new benchmark subsection, new results, involving multilayered plates, cylinders, cylindrical panels, and spherical shells for different thickness ratios, are presented and discussed in detail.

3.1 Preliminary cases

In this subsection, two preliminary cases are used as comparisons to evaluate the correctness of the 3D–u–θ–ϕ–ψ model. A simply-supported multilayered plate and a simply-supported multilayered spherical shell are taken into account. Due to a lack of studies in the literature about a fully coupled 3D thermo-magneto-electro-elastic model (four-field models) for flat and curved structures, comparisons are made considering a 3D thermo-electro-elastic reference and a 3D thermo-magneto-elastic reference, separately. The comparison results are obtained using a number $M = 300$ for mathematical layers and an order $N = 3$ for the exponential matrix as stated in the convergence analysis for the pure elastic problem in Brischetto [58].

In the first Preliminary Case (PC1), a multilayered simply-supported plate is taken into account. The multilayered configuration is a two-layered *PZT-5A*/*Cadmium Selenide* plate. Each layer thickness is equal to $0.5h$, where h is the total thickness of the structure. Material properties of *PZT-5A* and *Cadmium Selenide* in terms of elastic, electric, and thermal coefficients are collected in the first two columns of Table 1. Geometrical data are reported in the first column of Table 2. These two constituents do not have any magnetic coefficient as shown in Table 1. External loading boundary conditions for this case are: $\overline{\Theta}_t = 1, K$ and $\overline{\Theta}_b = 0, K$. No load conditions are imposed on the electric and elastic fields. Comparison results proposed in Table 3 are obtained considering as reference solution the 3D thermo-electro-elastic sampling surface model by Kulikov [59]. In Table 3, a perfect agreement is reached for both thickness ratios and for all normalized variables. Normalized variables are given as:

$$\overline{\theta} = \frac{\theta}{\overline{\Theta}_t}; \quad \overline{q}_z = \frac{10aq_z}{\frac{a}{h}k_0\overline{\Theta}_t}; \quad \overline{u} = \frac{10u}{a\alpha_0\overline{\Theta}_t};$$
$$\overline{w} = \frac{100w}{\frac{a}{h}a\alpha_0\overline{\Theta}_t}; \overline{\sigma}_{\alpha\alpha} = \frac{10\sigma_{\alpha\alpha}}{E_1\alpha_0\overline{\Theta}_t}; \quad \overline{\sigma}_{\alpha\beta} = \frac{10\sigma_{\alpha\beta}}{E_1\alpha_0\overline{\Theta}_t}; \tag{72}$$

$$\overline{\sigma}_{\alpha z} = \frac{10\frac{a}{h}\sigma_{\alpha z}}{E_1\alpha_0\overline{\Theta}_t}; \quad \overline{\sigma}_{zz} = \frac{10\left(\frac{a}{h}\right)^2\sigma_{zz}}{E_1\alpha_0\overline{\Theta}_t}; \tag{73}$$

where $k_0 = 9$ W/mK, $\alpha_0 = 4.396 \cdot 10^{-6}$ 1/K, and $E_1 = 42.785$ GPa. Thanks to the presented results, it is possible to confirm the correctness of the 3D–u–θ–ϕ–ψ model in depicting the

Table 1: Elasto-thermo-magneto-electric material properties used in the preliminary cases (PC) and new benchmarks (B).

	Cadmium Selenide [59]	PZT-5A [59]	Adaptive wood [60]	Soft adaptive wood [60]
E_1 [GPa]	42.785	61	154.32	77.16
E_2 [GPa]	42.785	61	154.32	77.16
E_3 [GPa]	57.707	53.199	142.83	71.415
ν_{12} [–]	0.4805	0.35	0.36564	0.18282
ν_{13} [–]	0.2442	0.38	0.40133	0.200665
ν_{23} [–]	0.2442	0.38	0.40133	0.200665
G_{12} [GPa]	14.45	22.593	56.5	28.25
G_{13} [GPa]	13.17	21.1	45.3	22.65
G_{23} [GPa]	13.17	21.1	45.3	22.65
α_{11} [10^{-6}] [1/K]	1.2566	1.5005	14.1	14.1
α_{22} [10^{-6}] [1/K]	1.2566	1.5005	14.1	14.1
α_{33} [10^{-6}] [1/K]	1.2566	1.9989	7.2	7.2
k_{11} [W/mK]	9	1.8	2.61	1.305
k_{22} [W/mK]	9	1.8	2.61	1.305
k_{33} [W/mK]	13.5	1.8	2.61	1.305
r_{15} [T]	–	–	560	280
r_{24} [T]	–	–	560	280
r_{31} [T]	–	–	580	290
r_{32} [T]	–	–	580	290
r_{33} [T]	–	–	700	350
μ_{11} [nH/m]	–	–	$\mp 590 \cdot 10^3$	$\mp 295 \cdot 10^3$
μ_{22} [nH/m]	–	–	$\mp 590 \cdot 10^3$	$\mp 295 \cdot 10^3$
μ_{33} [nH/m]	–	–	$157 \cdot 10^3$	$78.5 \cdot 10^3$
e_{15} [C/m^2]	−0.138	12.322	11.6	5.8
e_{24} [C/m^2]	−0.138	12.322	11.6	5.8
e_{31} [C/m^2]	−0.160	−7.209	−4.4	−2.2
e_{32} [C/m^2]	−0.160	−7.209	−4.4	−2.2
e_{33} [C/m^2]	0.347	15.118	18.6	9.3
ϵ_1 [nF/m]	0.0825	15.3	0.08	0.04
ϵ_2 [nF/m]	0.0825	15.3	0.08	0.04
ϵ_3 [nF/m]	0.0902	15	0.093	0.0465
d_1 [10^{-12} Ns/VC]	–	–	3	1.5
d_2 [10^{-12} Ns/VC]	–	–	3	1.5
d_3 [10^{-12} Ns/VC]	–	–	3	1.5
p_3 [10^{-6}] [C/m^{2}K]	−2.94	700	−130	−65
g_3 [10^{-3} A/mK]	–	–	6	3

thermo-electro-elastic coupling with related thickness and material layer effects.

In the second Preliminary Case (PC2), a multilayered simply-supported spherical shell is considered to validate the thermo-magneto-elastic coupling in curved structures.

Table 2: Geometrical data for structures analyzed in the preliminary case (PC) results.

	PC1	PC2
a [m]	1	$\frac{1}{6}\pi R_\alpha$
b [m]	1	$\frac{2}{9}\pi R_\beta$
R_α [m]	∞	3
R_β [m]	∞	3
h [m]	Variable	0.1
m	1	1
n	1	1

Table 3: PC1, simply-supported two-layered thermo-electro-elastic plate. $\bar{z}/h$ goes from 0 (bottom) to 1 (top).

a/h		2	10
$\overline{\theta}\ (\bar{z}/h = 0.00)$	3D [59]	0.6058	0.8675
	3D–u–θ–ϕ–ψ	0.6058	0.8675
$\overline{u}\ (\bar{z}/h = 0.50)$	3D [59]	−2.3801	−2.8455
	3D–u–θ–ϕ–ψ	−2.3811	−2.8450
$\overline{w}\ (\bar{z}/h = 0.50)$	3D [59]	10.215	6.2730
	3D–u–θ–ϕ–ψ	10.243	6.2934
$\overline{\sigma}_{\alpha\alpha}\ (\bar{z}/h = 0.50)$	3D [59]	−4.6432	−1.6989
	3D–u–θ–ϕ–ψ	−4.6372	−1.7031
$\overline{\sigma}_{\alpha\beta}\ (\bar{z}/h = 0.50)$	3D [59]	−5.0506	−6.0384
	3D–u–θ–ϕ–ψ	−5.0528	−6.0373
$\overline{\sigma}_{\alpha z}\ (\bar{z}/h = 0.00)$	3D [59]	1.3501	2.7132
	3D–u–θ–ϕ–ψ	1.3384	2.6833
$\overline{\sigma}_{zz}\ (\bar{z}/h = 0.00)$	3D [59]	−1.6477	−6.3876
	3D–u–θ–ϕ–ψ	−1.6388	−6.3522
$\overline{q}_z\ (\bar{z}/h = 0.00)$	3D [59]	−3.3465	−3.5268
	3D–u–θ–ϕ–ψ	−3.3465	−3.5268

The three-layered 0°/90°/0° configuration is the *Adaptive Wood*/*Soft Adaptive Wood*/*Adaptive Wood* lamination scheme. Outer laminae are $0.3h$ thick and the central one is $0.4h$ thick. h is the total thickness. Geometrical data are reported in the second column of Table 2. Material data for *Adaptive Wood* and *Soft Adaptive Wood* are collected in Table 1. In order to be consistent with the reference solution [60], the magnetic permittivity coefficients μ_{11} and μ_{22} are both considered with negative signs. The reference solution is the 2D refined Equivalent Layer Wise (ELW) model by Tornabene [60]. For this case, the load boundary conditions imposed at the outer surfaces of the structure are: $\overline{P}_{z_t} = -7 \cdot 10^5$ Pa, $\overline{P}_{z_b} = 3 \cdot 10^5$ Pa, $\overline{\Psi}_t = -800$ V, $\overline{\Phi}_b = 20$ V, $\overline{\Theta}_t = 10$ K, $\overline{\Theta}_b = 2$ K. In this case, the electric field is not considered. Table 4 compares results for in-plane and transverse displacements, magnetic potential, over-

Table 4: PC2, simply-supported three-layered thermo-magneto-elastic spherical shell. $\tilde{z}/h$ goes from 0 (bottom) to 1 (top).

		ELW [60]	3D–u–θ–ϕ–ψ
u [10^{-5} m]	$(\tilde{z}/h = 0.50)$	−3.919	−3.910
v [10^{-5} m]	$(\tilde{z}/h = 0.30)$	−3.273	−3.289
w [10^{-4} m]	$(\tilde{z}/h = 1.00)$	−1.280	−1.300
ψ [10^{2} A]	$(\tilde{z}/h = 0.50)$	−2.050	−2.074
θ [K]	$(\tilde{z}/h = 0.70)$	4.150	4.126
$\sigma_{\alpha\alpha}$ [10^{7} Pa]	$(\tilde{z}/h = 1.00)$	−1.650	−1.667
$\sigma_{\beta z}$ [10^{5} Pa]	$(\tilde{z}/h = 0.50)$	−5.000	−5.042
σ_{zz} [10^{4} Pa]	$(\tilde{z}/h = 0.50)$	8.850	8.147
$\mathscr{B}_{\alpha}$ [10^{-1} T]	$(\tilde{z}/h = 0.50)$	−1.471	−1.293

temperature, in-plane normal stress, transverse shear stress, transverse normal stress, and in-plane magnetic induction: the 2D ELW model by Tornabene [60] and the present 3D–u–θ–ϕ–ψ model are compared. Reference results are evaluated starting from the graphical trends available in [60]. Results coming from the 3D–u–θ–ϕ–ψ model are in very good agreement with the reference results; small differences are due to the fact that the 2D ELW results come from graphical evaluations. Therefore, it is possible to confirm the correctness of the 3D–u–θ–ϕ–ψ model to analyze the thermo-magneto-elastic coupling and related curvature, thickness, and material layer effects.

From the results obtained in the present subsection, the thermo-magneto-electro-elastic coupling can be considered correctly validated. This statement is possible as thermo-electro-elastic coupling and thermo-magneto-elastic coupling have been separately validated. In addition, the curvature effect, thickness layer effect, and material layer effect are depicted for both cases. The two proposed preliminary cases have been performed considering M = 300 mathematical layers and an order N = 3 for the exponential matrix. For this reason, the following new benchmark subsection will be presented considering these two key values for M and N parameters.

3.2 New benchmarks

In the present new Benchmark subsection, new multilayered cases are presented. Multilayered simply-supported plates, cylinders, cylindrical panels, and spherical shell cases are shown and discussed (see Figure 1 for the geometry). The multilayered configuration is the five-layered stacking sequence presented in Figure 2. The five-layered configuration is adopted for all four new benchmarks. Material properties of the two constituents (*Adaptive Wood* and *Soft Adaptive Wood*) are reported in the last two columns of Table 1 in terms of elastic, thermal, magnetic, and electric properties. The four new benchmarks have been proposed considering μ_{11} and μ_{22} with positive signs, as recommended in [61] to obtain a physically meaningful case. The load boundary conditions imposed at the outer surfaces for each proposed benchmark are the following:

$$\begin{aligned} &\overline{P}_{z_t} = 1{,}000 \text{ Pa}, \overline{P}_{z_b} = 0 \text{ Pa}, \quad \overline{\Theta}_t = 1 \text{ K}, \overline{\Theta}_b = 0\text{K}, \\ &\overline{\Phi}_t = 10 \text{ A}, \overline{\Psi}_t = 5 \text{ A}, \overline{\Psi}_b = 0 \text{ A}, \quad \overline{\Phi}_b = 0 \text{ A}, \end{aligned} \tag{74}$$

with half-wave numbers m and n indicated in the last two lines of Table 5.

In the first new Benchmark (B1), a simply-supported multilayered rectangular plate is analyzed. Geometrical data for the plate configuration are reported in Table 5. Table 6 shows values of u, w, ψ, ϕ, θ, $\sigma_{\alpha\beta}$, σ_{zz}, $\mathscr{B}_z$, $\mathscr{D}_z$ and q_z for a specific thickness location $\tilde{z}/h$, and for structures from thick (a/h = 2) to thin (a/h = 100) configurations. As expected, transverse displacement w increases monotonically going from thick to thin structures. The same increasing trend is

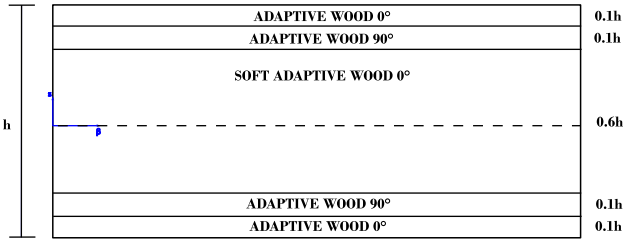

Figure 2: Multilayered lamination scheme adopted for the new benchmarks (B). Dotted lines indicate the middle reference surface Ω_0. h is the total thickness of the structure. The same lamination scheme is also used for curved structures.

Table 5: Geometrical data and half-wave numbers for structures analyzed in the new benchmark (B) results.

	B1	B2	B3	B4
a [m]	2	$2\pi R_{\alpha}$	$\frac{\pi}{3}R_{\alpha}$	$\frac{\pi}{3}R_{\alpha}$
b [m]	1	10	10	$\frac{\pi}{3}R_{\alpha}$
R_{α} [m]	∞	10	10	10
R_{β} [m]	∞	∞	∞	10
m	1	2	1	1
n	1	1	0	1

Table 6: B1, simply-supported multilayered elasto-thermo-magneto-electric rectangular plate. Results are obtained via the 3D–u–θ–ϕ–ψ model. $\widetilde{z}/h$ goes from 0 (bottom) to 1 (top).

a/h	2	4	10	20	50	100
			u [10^{-7} m] ($\widetilde{z}/h = 0.50$)			
	−4.8942	−9.5370	−11.785	−12.150	−12.217	−12.159
			w [10^{-6} m] ($\widetilde{z}/h = 0.50$)			
	1.2818	3.2622	8.7459	17.837	47.862	118.11
			ψ [A] ($\widetilde{z}/h = 0.85$)			
	−4.2146	−2.0312	1.3521	2.9058	3.8685	4.1705
			ϕ [A] ($\widetilde{z}/h = 0.15$)			
	381.88	264.21	104.54	68.728	75.712	122.71
			θ [K] ($\widetilde{z}/h = 0.50$)			
	0.1999	0.3811	0.4774	0.4942	0.4991	0.4998
			$\sigma_{\alpha\beta}$ [10^3 Pa] ($\widetilde{z}/h = 0.15$)			
	−22.771	−62.234	−85.235	−85.607	−60.871	28.763
			σ_{zz} [Pa] ($\widetilde{z}/h = 0.85$)			
	−6624.6	−3724.7	−47.756	679.73	892.11	922.31
			$\mathscr{B}_z$ [T] ($\widetilde{z}/h = 1.00$)			
	0.0109	0.0082	0.0050	0.0026	−0.0046	−0.0168
			$\mathscr{D}_z$ [10^{-6} C/m^2] ($\widetilde{z}/h = 1.00$)			
	9.4020	7.6801	6.5596	5.8327	3.8504	0.4887
			q_z [W/m^2] ($\widetilde{z}/h = 1.00$)			
	−7.8083	−7.1168	−9.8385	−17.165	−41.124	−81.734

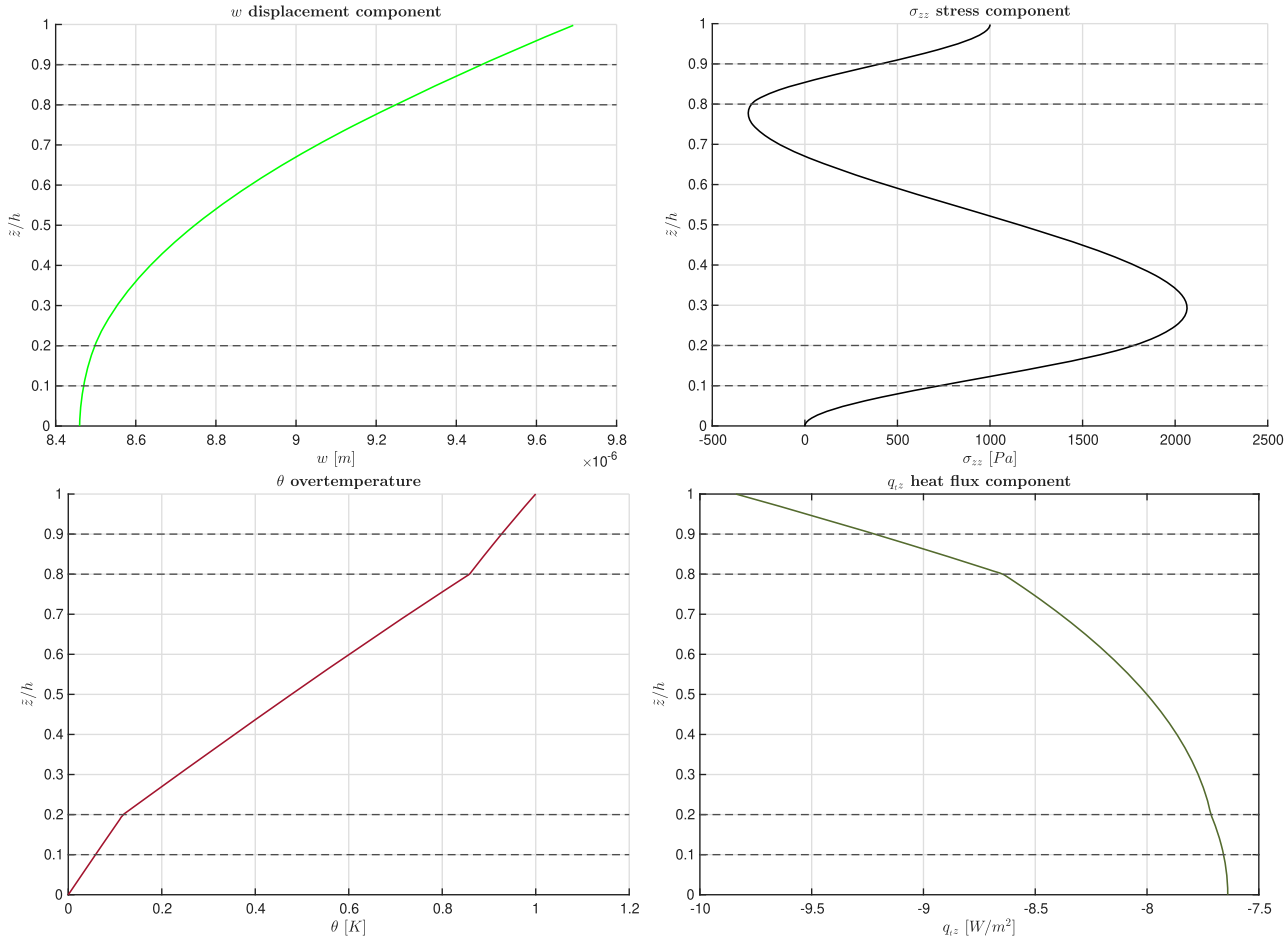

Figure 3: B1, simply-supported multilayered elasto-thermo-magneto-electric rectangular plate. Results are obtained via the 3D-u–θ–ϕ–ψ model. $\widetilde{z}/h$ goes from 0 (bottom) to 1 (top). Thickness ratio is a/h = 10.

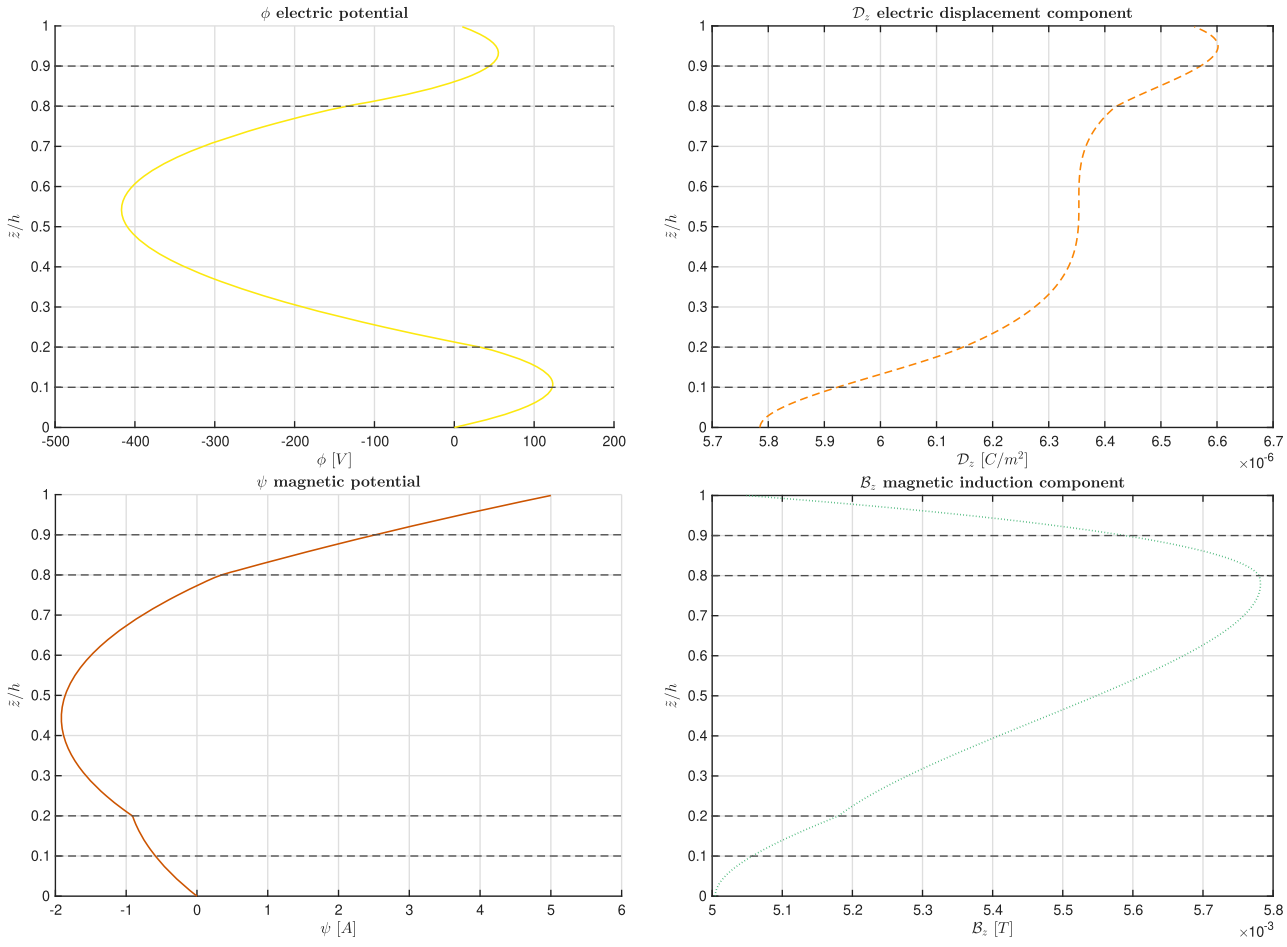

Figure 3: Continued.

Table 7: B2, simply-supported multilayered elasto-thermo-magneto-electric cylinder. Results are obtained via the 3D–u–θ–ϕ–ψ model. $\tilde{z}/h$ goes from 0 (bottom) to 1 (top).

R_a/h	2	4	10	20	50	100
			u [10^{-6} m] ($\tilde{z}/h = 0.50$)			
	3.6527	8.3228	13.118	12.178	10.365	10.360
			w [10^{-5} m] ($\tilde{z}/h = 0.50$)			
	4.3141	7.6048	10.371	9.9911	9.1229	9.1048
			ψ [A] ($\tilde{z}/h = 0.85$)			
	−57.189	−33.735	−9.7999	−1.7655	2.2485	3.4212
			ϕ [10^3 A] ($\tilde{z}/h = 0.15$)			
	0.8095	−8.0185	−11.262	−7.7947	−3.5675	−1.8529
			θ [K] ($\tilde{z}/h = 0.50$)			
	0.3935	0.4694	0.4949	0.4987	0.4998	0.4999
			$\sigma_{\beta\beta}$ [10^5 Pa] ($\tilde{z}/h = 0.15$)			
	0.9516	5.0594	18.080	25.719	29.805	31.003
			σ_{zz} [10^4 Pa] ($\tilde{z}/h = 0.85$)			
	4.2330	2.4876	2.1932	1.7067	0.8995	0.5161
			$\mathscr{B}_z$ [10^{-2} T] ($\tilde{z}/h = 1.00$)			
	1.2492	0.9442	0.8085	0.7567	0.6083	0.3609
			$\mathscr{D}_z$ [10^{-5} C/m^2] ($\tilde{z}/h = 1.00$)			
	0.2102	−2.6467	−4.5870	−4.4176	−4.0386	−4.1232
			q_z [W/m^2] ($\tilde{z}/h = 1.00$)			
	−0.6624	−0.8343	−1.7060	−3.3001	−8.1713	−16.320

visible for another primary variable of the thermo-magneto-electro-elastic problem: the sovra-temperature θ. Figure 3 shows the trend of w, ψ, ϕ, θ, σ_{zz}, $\mathcal{B}_z$, $\mathcal{D}_z$ and q_z variables through the thickness of a moderately thick plate (a/h = 10). Some effects acting on thermo-magneto-electro-elastic structures can be seen: thermo-magneto-electro-elastic coupling, zig-zag effect, material layer effect, and thickness layer effect. Thermo-magneto-electro-elastic coupling is visible considering the non-zero behavior of all the primary variables. Zig-zag effect is visible as slope changes within each physical layer. Material layer effect and thickness layer effect can be seen considering the different trends within each physical layer and the complex behavior along the thickness direction, respectively. In addition, external loading boundary conditions are correctly reached at the outer surfaces. This can be seen in σ_{zz}, θ, ϕ and ψ variable values at the outer surfaces. All the proposed variables are continuous along the thickness direction because interlaminar continuity conditions are correctly imposed between adjacent layers.

The second new Benchmark (B2) involves a simply-supported multilayered cylinder. Geometrical data are reported in Table 5. Table 7 shows u, w, ψ, ϕ, θ, $\sigma_{\beta\beta}$, σ_{zz}, $\mathcal{B}_z$, $\mathcal{D}_z$ and q_z variables for specific $\bar{z}/h$ thickness locations and for six different thickness ratios. In Table 7, w shows a non-monotonic behavior when increasing the thickness ratio because of the curvature effect. This is a typical trend for curved structures, indicating the presence of the curvature effect. In Figure 4, the trend along the thickness direction for w, ϕ, ψ, θ, σ_{zz}, $\mathcal{D}_z$, $\mathcal{B}_z$ and q_z is shown for R_a/h = 20. It is clearly

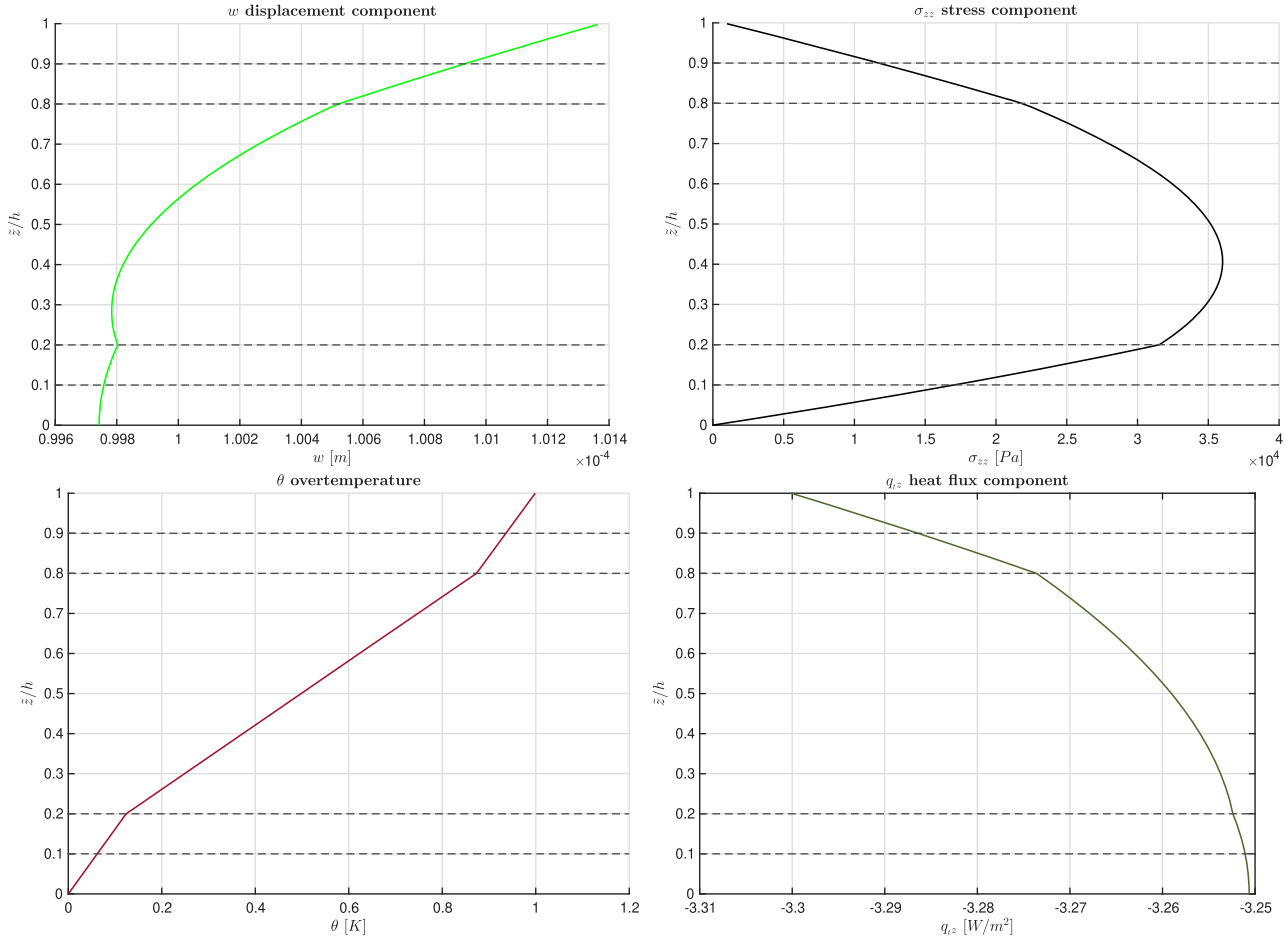

Figure 4: B2, simply-supported multilayered elasto-thermo-magneto-electric cylinder. Results are obtained via the 3D–u–θ–ϕ–ψ model. $\bar{z}/h$ goes from 0 (bottom) to 1 (top). Thickness ratio is R_a/h = 20.

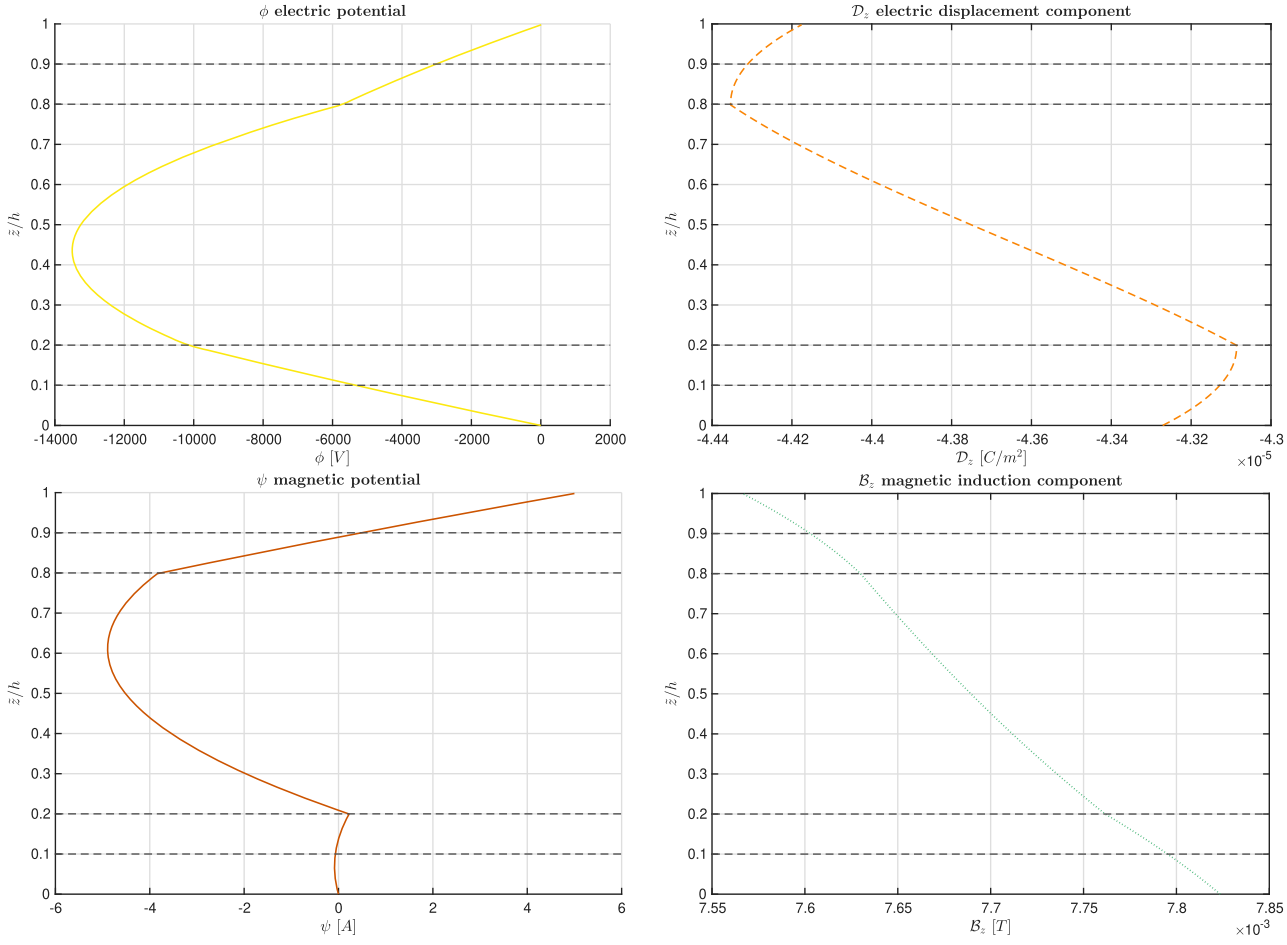

Figure 4: Continued.

visible that the zig-zag effect, the thermo-electro-elastic coupling, and the material and thickness layer effects are present: complex trends along the thickness direction are shown. Interlaminar continuity conditions are correctly imposed: trends in Figure 4 do not show discontinuities along the z direction. In addition, external loading boundary conditions are correctly reached at the outer surfaces, as shown by the transverse normal stress ($\overline{P}_{z_t} = 1,000$ Pa, $\overline{P}_{z_b} = 0$ Pa), over-temperature ($\overline{\Theta}_t = 1$ K, $\overline{\Theta}_b = 0$ K), electric potential ($\overline{\Phi}_t = 10$ A, $\overline{\Phi}_b = 0$ A), and magnetic potential ($\overline{\Psi}_t = 5$ A, $\overline{\Psi}_b = 0$ A) values at the outer surfaces.

For the third new Benchmark (B3), a simply-supported multilayered cylindrical panel is analyzed. Table 5 gives the geometrical data used for this case. Variables u, w, ψ, ϕ, θ, $\sigma_{\alpha\alpha}$, σ_{zz}, $\mathcal{B}_z$, $\mathcal{D}_z$ and q_z are proposed for a specific $\bar{z}/h$ thickness location and for different thickness ratios going from thick to thin ones. Curvature effects can be seen from the non-monotonic trend of some variables (such as the electric potential ϕ) when the thickness ratio increases. In Figure 5, it is possible to visualize the thickness layer effect considering the different complex trends for σ_{zz} and ψ with respect to the previous two benchmarks ($R_\alpha/h = 4$ is a thick cylindrical panel). No tabular and graphical trends involving the β direction are reported because $n = 0$ is imposed for this case. Thermo-magneto-electro-elastic coupling is correctly depicted considering primary variable trends along the thickness direction. Zig-zag effect is visible for each variable reported in Figure 5 considering the slope changes for each physical layer. Graphical trends are continuous along the thickness direction: this feature

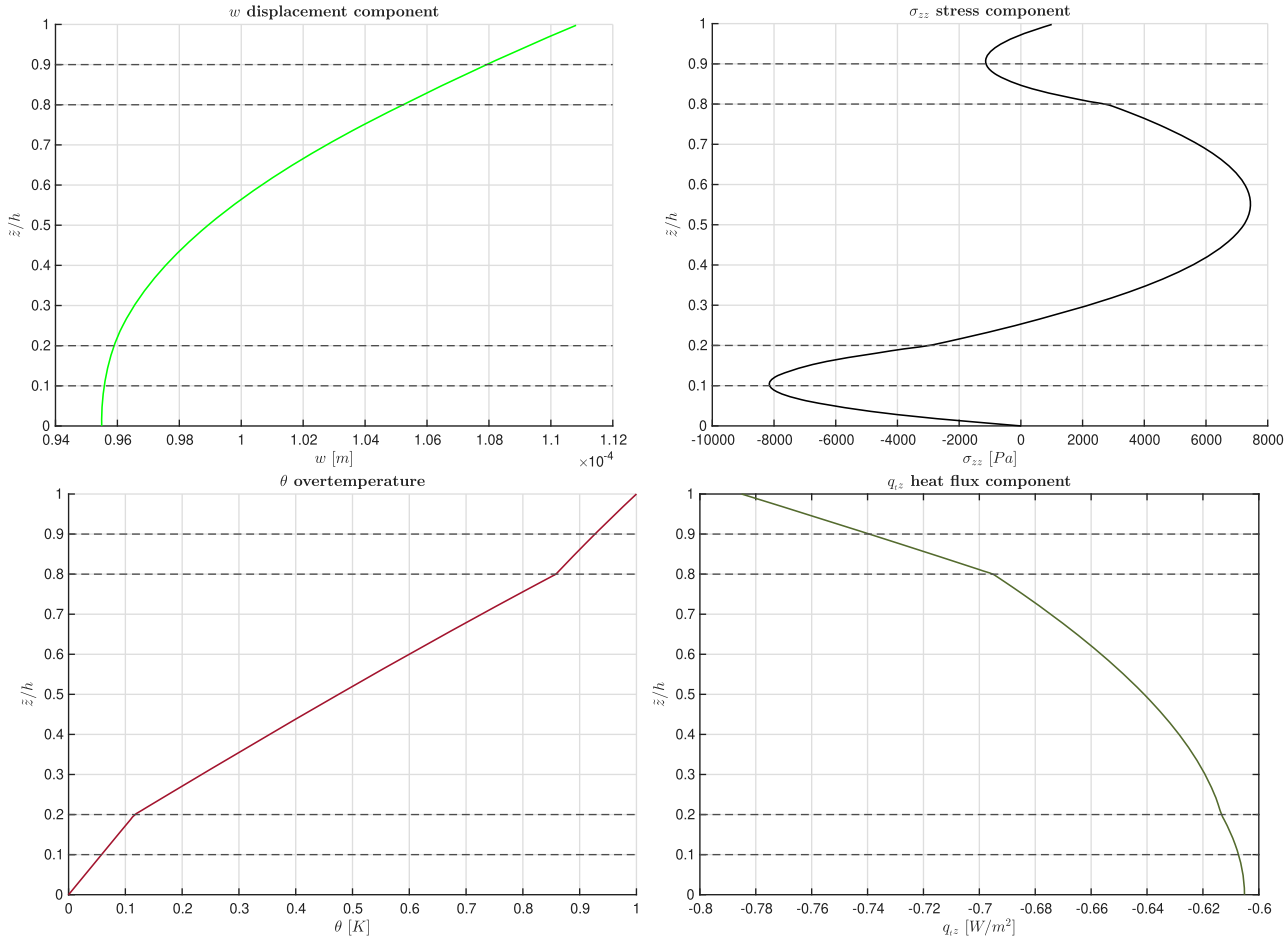

Figure 5: B3, simply-supported multilayered elasto-thermo-magneto-electric cylindrical shell panel. Results are obtained via the 3D–u–θ–ϕ–ψ model. $\bar{z}/h$ goes from 0 (bottom) to 1 (top). Thickness ratio is $R_\alpha/h = 4$.

indicates the correctness of imposing the interlaminar continuity conditions between adjacent layers as done in Eqs. (47) and (48). Loading boundary conditions are correctly reached at the outer surfaces as can be seen from σ_{zz}, ψ, ϕ and θ graphical trends at the top and bottom of the panel.

In the last Benchmark (B4), a simply-supported multilayered spherical panel is proposed. The last column of Table 5 collects the geometrical data used for this benchmark. In Tables 8 and 9, values of $u, w, \psi, \phi, \theta, \sigma_{\alpha\beta}, \sigma_{zz}, \mathcal{B}_z, \mathcal{D}_z$ and q_z are calculated for a specific thickness location for thick, moderately thick, moderately thin, and thin structures. In Table 9, the curvature effect can be seen from the w displacement trend: it is not increasing monotonically going from thick to thin configurations. Figure 6 shows the main peculiarities involved in thermo-magneto-electro-elastic curved multilayered structures: thermo-magneto-electro-elastic coupling, zig-zag effect, curvature effect, material layer effect, and thickness layer effect. Zig-zag effect is visible as slope changes for each physical layer. Thermo-magneto-electro-elastic coupling is obvious as trends for displacements, magnetic potential, electric potential, and sovra-temperature are different from zero. Interlaminar continuity conditions and loading boundary conditions are correctly imposed: in Figure 6, variables are continuous along the thickness direction and σ_{zz}, θ, ϕ and ψ trends have the proper imposed values written in Eq. (74) at the outer surfaces.

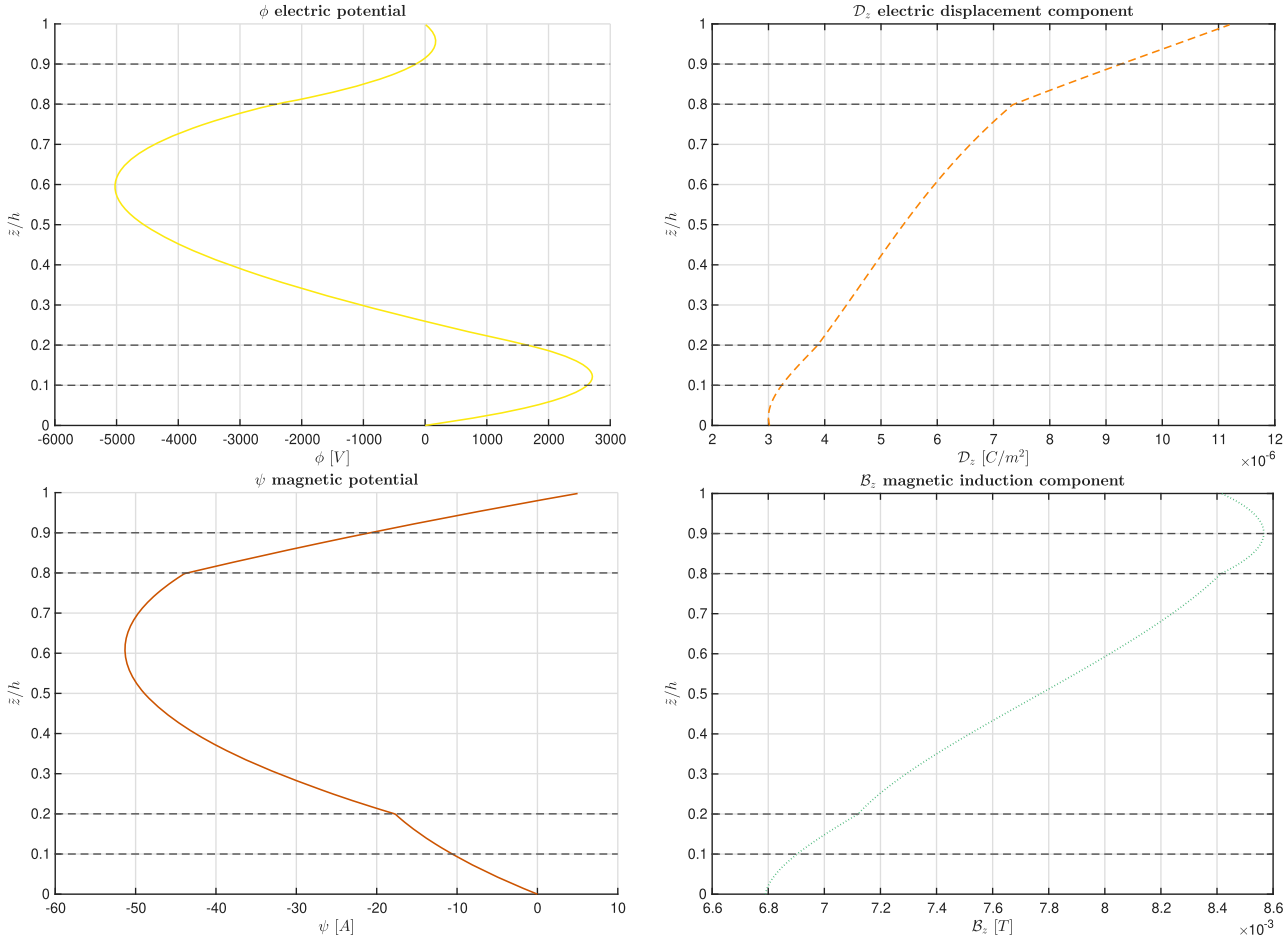

Figure 5: Continued.

Table 8: B3, simply-supported multilayered elasto-thermo-magneto-electric cylindrical shell panel. Results are obtained via the 3D–u–θ–ϕ–ψ model. $\tilde{z}/h$ goes from 0 (bottom) to 1 (top).

R_α/h	2	4	10	20	50	100
			u [10^{-5} m] ($\tilde{z}/h = 0.50$)			
	−1.4513	0.0801	5.6891	16.179	66.448	283.14
			w [10^{-5} m] ($\tilde{z}/h = 0.50$)			
	4.3830	9.8912	26.845	58.278	209.04	859.09
			ψ [A] ($\tilde{z}/h = 0.85$)			
	−60.374	−33.038	−11.395	−3.6748	0.6858	1.6047
			ϕ [10^3 A] ($\tilde{z}/h = 0.15$)			
	7.0548	2.5736	1.0204	1.0056	1.9019	3.6284
			θ [K] ($\tilde{z}/h = 0.50$)			
	0.4153	0.4755	0.4958	0.4989	0.4998	0.5000
			$\sigma_{\alpha\alpha}$ [10^5 Pa] ($\tilde{z}/h = 0.15$)			
	0.9489	1.0666	0.6010	−1.2659	−14.200	−60.061
			σ_{zz} [10^3 Pa] ($\tilde{z}/h = 0.85$)			
	5.3253	−0.0544	−1.0840	−1.8336	−4.8352	−10.245
			$\mathscr{B}_z$ [10^{-2} T] ($\tilde{z}/h = 1.00$)			
	1.0114	0.8416	0.7568	0.7066	0.5613	0.3127
			$\mathscr{D}_z$ [10^{-6} C/m^2] ($\tilde{z}/h = 1.00$)			
	14.192	11.195	8.8021	7.7999	6.7490	5.6600
			q_z [W/m^2] ($\tilde{z}/h = 1.00$)			
	−0.5472	−0.7851	−1.6899	−3.2928	−8.1686	−16.319

Table 9: B4, simply-supported multilayered elasto-thermo-magneto-electric spherical shell panel. Results are obtained via the 3D–u–θ–ϕ–ψ model. $\bar{z}/h$ goes from 0 (bottom) to 1 (top).

R_α/h	2	4	10	20	50	100
			u [10^{-6} m] ($\bar{z}/h = 0.50$)			
	−4.5679	−2.4067	5.2176	6.3754	4.4426	3.9586
			w [10^{-5} m] ($\bar{z}/h = 0.50$)			
	2.6229	5.2774	8.9607	9.4744	8.6392	8.4148
			ψ [A] ($\bar{z}/h = 0.85$)			
	−53.930	−33.107	−10.934	−2.2445	2.1689	3.4028
			ϕ [10^{3} A] ($\bar{z}/h = 0.15$)			
	12.249	0.1704	−7.5951	−6.7993	−3.4466	−1.8252
			θ [K] ($\bar{z}/h = 0.50$)			
	0.3517	0.4529	0.4917	0.4979	0.4997	0.4999
			$\sigma_{\alpha\beta}$ [10^{5} Pa] ($\bar{z}/h = 0.15$)			
	1.8123	3.8630	5.3000	4.0112	2.1553	1.6506
			σ_{zz} [10^{4} Pa] ($\bar{z}/h = 0.85$)			
	4.5433	1.6076	2.3256	2.6412	1.6108	0.9277
			$\mathcal{B}_z$ [10^{-3} T] ($\bar{z}/h = 1.00$)			
	12.519	9.7246	8.0577	7.5477	6.0900	3.6140
			$\mathcal{D}_z$ [10^{-5} C/m^2] ($\bar{z}/h = 1.00$)			
	1.9858	−1.0597	−4.1549	−4.5657	−4.1920	−4.1778
			q_z [W/m^2] ($\bar{z}/h = 1.00$)			
	−0.7401	−0.9124	−1.7482	−3.3230	−8.1809	−16.325

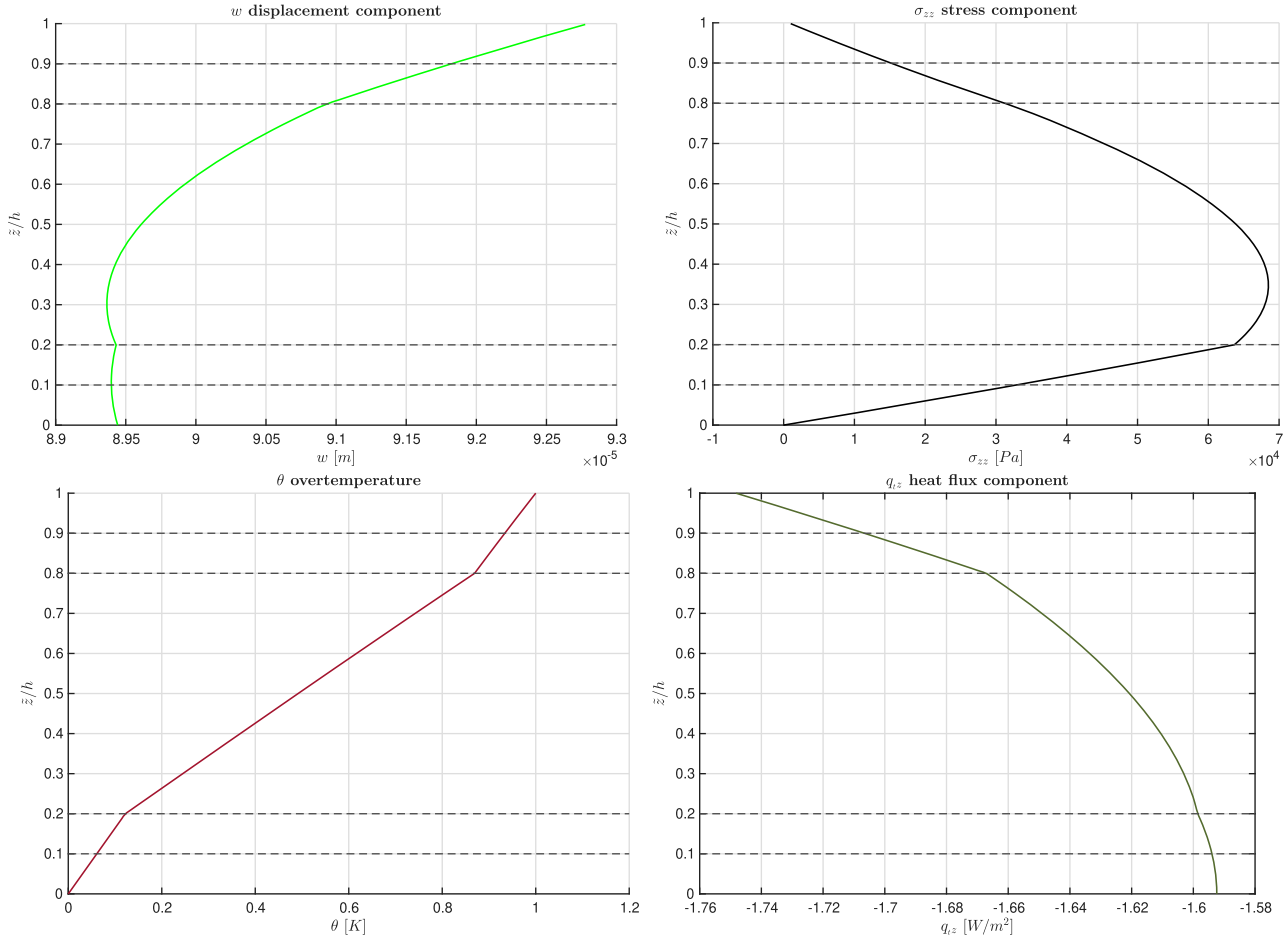

Figure 6: B4, simply-supported multilayered elasto-thermo-magneto-electric spherical shell panel. Results are obtained via the 3D–u–θ–ϕ–ψ model. $\bar{z}/h$ goes from 0 (bottom) to 1 (top). Thickness ratio is R_α/h = 10.

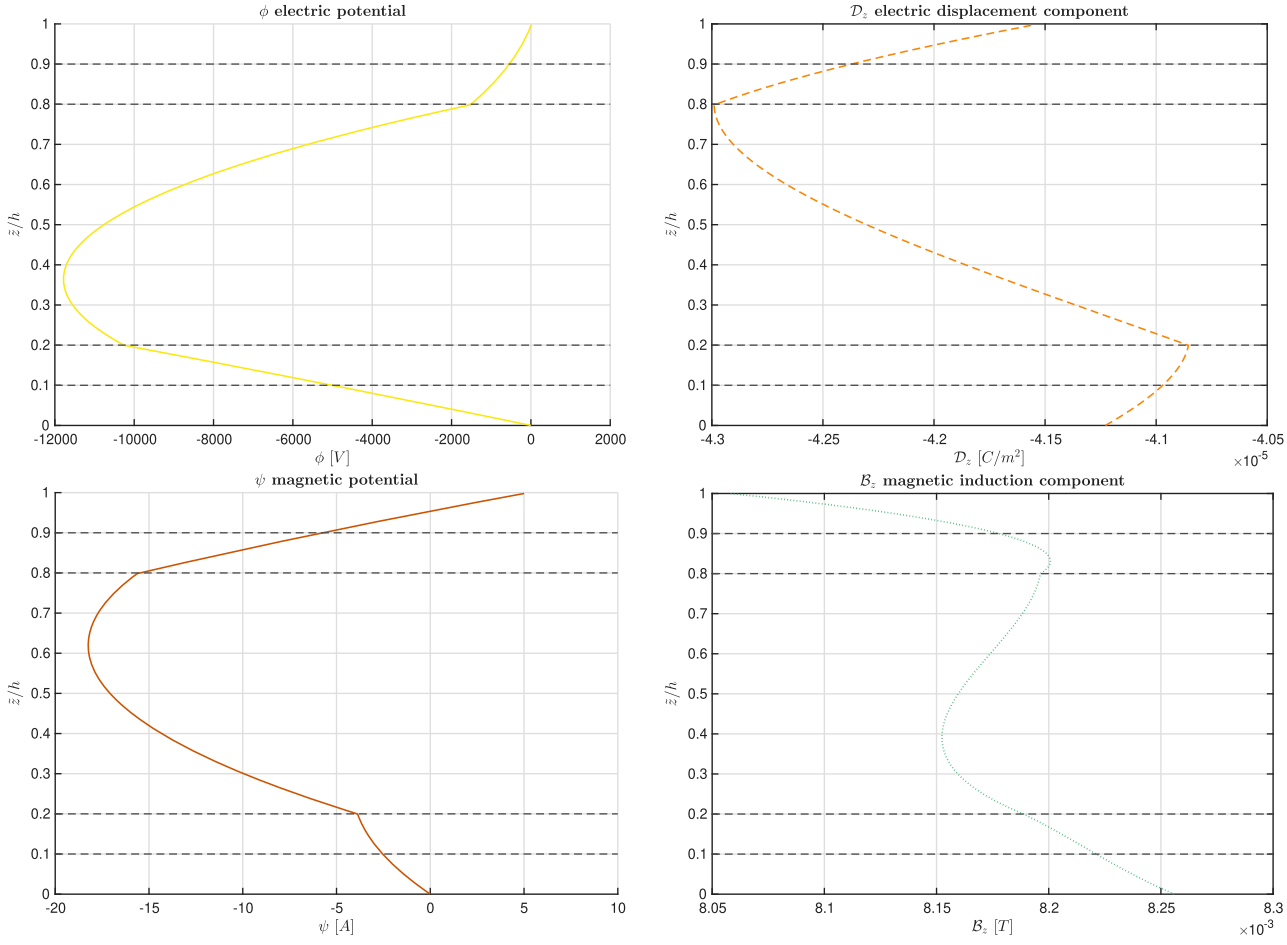

Figure 6: Continued.

4 Conclusions

This study focuses on the fully coupled 3D static analysis of thermo-magneto-electro-elastic multilayered plates and shells. The six 3D governing equations associated with the thermo-magneto-electro-elastic spherical shell problem have been formulated. 3D multifield constitutive equations and 3D geometrical relations for spherical shells are used to describe the material properties and the structural kinematics. The six 3D thermo-magneto-electro-elastic spherical shell equations are solved by employing Navier harmonic forms in the in-plane directions and the exponential matrix method along the thickness direction. The six 3D governing equations are formulated within a mixed curvilinear orthogonal reference system, thus enabling the analysis of different geometries, including plates, cylinders, cylindrical panels, and spherical shells. Interlaminar continuity conditions are introduced between adjacent layers on displacements, magnetic potential, electric potential, over-temperature, transverse shear and normal stresses, transverse normal magnetic induction, transverse normal electric displacement, and transverse normal heat flux. These interlaminar continuity conditions enable the implementation of the layer-wise approach.

In the Results section, two preliminary cases are examined to assess the accuracy of the proposed 3D thermo-magneto-electro-elastic model through comparison with 3D and quasi-3D thermo-magneto-elastic and thermo-electro-elastic models available in the literature. The comparison demonstrates excellent agreement in terms of tabulated results. Furthermore, the results confirm the correct representation of zig-zag effects, thermo-magneto-electro-elastic coupling, curvature effects, material effects, and layer-thickness effects. Based on the outcomes obtained in the preliminary validation study, four new benchmark cases have been introduced for different thickness ratios and four distinct geometries: plates, cylinders, cylindrical panels, and spherical shells. In the benchmark subsection, several results have been obtained at selected thickness locations

spanning from thick to thin configurations. Through-the-thickness graphical distributions have also been reported for representative thickness ratios. In this way, zig-zag effects, thermo-magneto-electro-elastic coupling, curvature effects, material effects, and layer-thickness effects can be clearly identified and quantified. Interlaminar continuity conditions and loading boundary conditions have been consistently enforced throughout the model. The four-field coupling formulation has been successfully validated, and the proposed 3D thermo-electro-magneto-elastic shell model can therefore be reliably employed for future benchmark investigations.

The present work provides a useful reference framework for researchers interested in understanding the behavior of multilayered shell and plate structures subjected to static multifield loading conditions. Moreover, the 3D solutions presented herein may serve as benchmark results for the verification and assessment of multifield numerical and analytical 2D/3D models.

Research ethics: Not applicable.
Informed consent: Not applicable.
Author contributions: All authors have accepted responsibility for the entire content of this manuscript and approved its submission. Conceptualization: SB Methodology: SB Software: SB, DC Validation: DC Formal analysis: DC Investigation: DC Resources: SB Data curation: SB Writing – original draft: DC Writing – review & editing: SB.
Use of Large Language Models, AI and Machine Learning Tools: No Large Language Models, AI, and Machine Learning Tools were used in this study.
Conflict of interest: The authors declare that they have no conflict of interest.
Research funding: None declared.
Data availability: Not applicable.

References

1. Badri TM, Al-Kayiem HH. Analytical solution for simply-supported and multilayered magneto-thermo-electro-elastic plates. Asian J Sci Res 2013;6:236–44.
2. Shi S, Li P, Jin F. The establishment of coupled magneto-electro-thermo-elastic theory with the consideration of surface and non-local effects and its application in laminated nano-devices. Compos Struct 2017;179:541–51.
3. Starkov IA, Starkov AS. Effective parameters of multilayered thermo-electro-magneto-elastic solids. Solid State Commun 2016;226:5–7.
4. Wang S, Hong J, Gu S, Xiao Z, Zhang G. A size-dependent isogeometric model for magneto-electro-elastic graded curved beams in advanced structures. Compos Struct 2025;358:118877.
5. Xiong S-M, Ni G-Z. 2D Green's functions for semi-infinite transversely isotropic electro-magneto-thermo-elastic composite. J Magn Magn Mater 2009;321:1867–74.
6. Chang D-M, Liu X-F, Wang B-L, Liu L, Wang T-G, Wang Q, et al. Exact solutions to magneto-electro-thermo-elastic fields for a cracked cylinder composite during thermal shock. Int J Mech Mater Des 2020;16:3–18.
7. Ansari R, Gholami R, Rouhi H. Size-dependent nonlinear forced vibration analysis of magneto-electro-thermo-elastic Timoshenko nanobeams based upon the nonlocal elasticity theory. Compos Struct 2015;126:216–26.
8. Ansari R, Hasrati E, Gholami R, Sadeghi F. Nonlinear analysis of forced vibration of nonlocal third-order shear deformable beam model of magneto-electro-thermo-elastic nanobeams. Composites Part B 2015;83:226–41.
9. Badri Albarody TM, Al-Kayiem HH. Dynamic analysis of laminated composite thermo-magneto-electro-elastic shells. J Mech Sci Technol 2014;28:4877–91.
10. Ebrahimi F, Reza Barati M. Nonlocal thermal buckling analysis of embedded magneto-electro-thermo-elastic nonhomogeneous nanoplates. Iran J Sci Technol Trans Mech Eng 2016;40:243–64.
11. Esen I, Özmen R. Thermal vibration and buckling of magneto-electro-elastic functionally graded porous nanoplates using nonlocal strain gradient elasticity. Compos Struct 2022;296:115878.
12. Ghadiri M, Safarpour H. Free vibration analysis of embedded magneto-electro-thermoelastic cylindrical nanoshell based on the modified couple stress theory. Appl Phys A 2016;122:1–11.
13. Gui Y, Li Z. A nonlocal strain gradient shell model with the surface effect for buckling analysis of a magneto-electro-thermo-elastic cylindrical nanoshell subjected to axial load. Phys Chem Chem Phys 2023;25:24838–52.
14. Gui Y, Wu R. Buckling analysis of embedded thermo-magneto-electro-elastic nano cylindrical shell subjected to axial load with nonlocal strain gradient theory. Mech Res Commun 2023;128:104043.
15. Lang Z, Xuewu L. Buckling and vibration analysis of functionally graded magneto-electro-thermo-elastic circular cylindrical shells. Appl Math Model 2013;37:2279–92.
16. Li Z, Wang Q, Qin B, Zhong R, Yu H. Vibration and acoustic radiation of magneto-electro-thermo-elastic functionally graded porous plates in the multi-physics fields. Int J Mech Sci 2020;185:105850.
17. Liu M-F, Yong C-H, Guo Y-M. Free vibration for the thermo-magneto-electro-elastic (TMEE) nanobeams based on modified couple stress theory. Mech Adv Mater Struct 2025;32:153–68.
18. Liu Y, Qin Z, Chu F. Investigation of magneto-electro-thermo-mechanical loads on nonlinear forced vibrations of composite cylindrical shells. Commun Nonlinear Sci Numer Simul 2022;107:106146.
19. Ni Y, Zhu S, Sun J, Tong Z, Zhou Z, Xu X. Analytical buckling solution of magneto-electro-thermo-elastic cylindrical shells under multi-physics fields. Compos Struct 2020;239:112021.
20. G-L She and L-L Gan, Nonlinear combined resonance of thermo-magneto-electro-elastic cylindrical shells. Dynamics 2025;5:48.
21. Zafari H, Tarkashvand A, Mukhopadhyay T. Transient dynamics and stress evolution under moving heat flux: a coupled magneto-electro-thermoelastic framework for smart hybrid plates resting on viscoelastic foundation. Mech Base Des Struct Mach 2025;53:7613–61.
22. Shojaeefard MH, Mahinzare M, Safarpour H, Saeidi Googarchin H, Ghadiri M. Free vibration of an ultra-fast-rotating-induced cylindrical nano-shell resting on a Winkler foundation under thermo-electro-magneto-elastic condition. Appl Math Model 2018;61:255–79.
23. Singh AK, Jaiswal R. Analysis on transverse vibration of piezo-electro-magneto-thermoelastic composite nanobeams under distinct Green–Naghdi III phase lag models. Eur J Mech Solid 2025;113:105702.

24. Zheng Y-F, Liu L-C, Qu D-Y, Chen C-P. Nonlinear postbuckling analysis of magneto-electro-thermo-elastic laminated microbeams based on modified couple stress theory. Appl Math Model 2023;118:89–106.
25. Arefi M, Zenkour AM. Vibration and bending analyses of magneto–electro–thermoelastic sandwich microplates resting on viscoelastic foundation. Appl Phys A 2017;123:1–17.
26. Mahesh V, Sagar PJ, Kattimani S. Influence of coupled fields on free vibration and static behavior of functionally graded magneto-electro-thermo-elastic plate. J Intell Mater Syst Struct 2017;29:1430–55.
27. Ren Y-M, Qing H. Size-dependent buckling and vibration of functionally graded magneto-electro-thermo-elastic Timoshenko nanobeams using general stress-driven two-phase local/nonlocal integral model. Thin-Walled Struct 2025;215:113480.
28. Aboudi J. The electric, magnetic, and elastic fields in damaged thermo-electro-magneto-elastic composites created by heat flow. J Intell Mater Syst Struct 2018;29:1670–84.
29. Akbarzadeh A, Chen Z. Thermo-magneto-electro-elastic responses of rotating hollow cylinders. Mech Adv Mater Struct 2014;21:67–80.
30. Arefi M, Zenkour AM. Effect of thermo-magneto-electro-mechanical fields on the bending behaviors of a three-layered nanoplate based on sinusoidal shear deformation plate theory. J Sandw Struct Mater 2019; 21:639–69.
31. Arefi M, Zenkour AM. Thermo-electro-magneto-mechanical bending behavior of size-dependent sandwich piezomagnetic nanoplates. Mech Res Commun 2017;84:27–42.
32. Barati AR, Shariyat M. Exact closed-form solutions for behavior investigation of heterogeneous piezo-magneto-elastic discs under magneto-electro-hygro-thermo-mechanical loads. Eur J Mech Solid 2023;101:105066.
33. Chen WQ, Lee KY, Ding HJ. General solution for transversely isotropic magneto-electro-thermo-elasticity and the potential theory method. Int J Eng Sci 2004;42:1361–79.
34. Dai HL, Wang X. Magneto–thermo–electro–elastic transient response in a piezoelectric hollow cylinder subjected to complex loadings. Int J Solid Struct 2006;43:5628–46.
35. Li P-D, Li X-Y, Kang G-Z, Müller R. Three-dimensional fundamental solution of a penny-shaped crack in an infinite thermo-magneto-electro-elastic medium with transverse isotropy. Int J Mech Sci 2017;130:203–20.
36. Li XY, Dong YH, Liu C, Liu Y, Wang CJ, Shi TF. Axisymmetric thermo-magneto-electro-elastic field in a heterogeneous circular plate subjected to a uniform thermal load. Int J Mech Sci 2014;88:71–81.
37. Li Y, Dang H-Y, Xu G-T, Fan C-Y, Zhao M-H. Extended displacement discontinuity boundary integral equation and boundary element method for cracks in thermo-magneto-electro-elastic media. Smart Mater Struct 2016;25:085048.
38. Serpilli M. Asymptotic interface models in magneto-electro-thermo-elastic composites. Meccanica 2017;52:1407–24.
39. Sobhy M. Magneto-electro-thermal bending of FG-graphene reinforced polymer doubly-curved shallow shells with piezoelectromagnetic faces. Compos Struct 2018;203:844–60.
40. Tong ZH, Lo SH, Jiang CP, Cheung YK. An exact solution for the three-phase thermo-electro-magneto-elastic cylinder model and its application to piezoelectric–magnetic fiber composites. Int J Solid Struct 2008;45:5205–19.
41. Tornabene F, Viscoti M, Dimitri R. Equivalent layer-wise theory for the hygro-thermo-magneto-electro-elastic analysis of laminated curved shells. Thin-Walled Struct 2024;198:111751.
42. Vinyas M, Kattimani SC. Influence of coupled material properties of BaTiO3 and CoFe2O4 on the static behavior of thermo-mechanically loaded magneto-electro-elastic beam. Mater Today Proc 2018;5: 7410–19.
43. Vinyas M, Kattimani SC. Investigation of the effect of $BaTiO_3/CoFe_2O_4$ particle arrangement on the static response of magneto-electro-thermo-elastic plates. Compos Struct 2018;185:51–64.
44. Vinyas M, Kattimani SC. Static analysis of stepped functionally graded magneto-electro-elastic plates in thermal environment: a finite element study. Compos Struct 2017;178:63–86.
45. Yang J, Jin X, Jin N. A penny-shaped crack in transversely isotropic magneto-electro-thermo-elastic medium subjected to uniform symmetric heat flux. Int J Solid Struct 2014;51:1792–808.
46. Zhou L, Yang H, Ma L, Zhang S, Li X, Ren S, et al. On the static analysis of inhomogeneous magneto-electro-elastic plates in thermal environment via element-free Galerkin method. Eng Anal Bound Elem 2022;134:539–52.
47. Zhou L, Li M, Ma Z, Yang H, Ren S, Li X, et al. Steady-state characteristics of the coupled magneto-electro-thermo-elastic multi-physical system based on cell-based smoothed finite element method. Compos Struct 2019;219:111–28.
48. Zhou L, Liang G, Wang J, Zhu P. The adaptive thermo-mechanical-electro-magnetic enriched finite element method for statics analysis of functionally graded magneto-electro-elastic structures. Finite Elem Anal Des 2026;253:104476.
49. Zhang XL, Xu Q, Zhao X, Li YH, Yang J. Nonlinear analyses of magneto-electro-elastic laminated beams in thermal environments. Compos Struct 2020;234:111524.
50. Brischetto S, Torre R, Cesare D. Three dimensional coupling between elastic and thermal fields in the static analysis of multilayered composite shells. Comput Model Eng Sci 2023;136:2551–94.
51. Brischetto S, Torre R, Cesare D. A layer-wise coupled thermo-elastic shell model for three-dimensional stress analysis of functionally graded material structures. Technologies 2023;11:35.
52. Brischetto S, Cesare D. 3D electro-elastic static analysis of advanced plates and shells. Int J Mech Sci 2024;280:109620.
53. Brischetto S, Cesare D. A 3D shell model for static and free vibration analysis of multilayered magneto-elastic structures. Thin-Walled Struct 2025;206:112620.
54. Brischetto S, Cesare D, Mondino T. 3D exact magneto-electro-elastic static analysis of multilayered plates. Comput Model Eng Sci 2025;144: 643–68.
55. Brischetto S, Cesare D, Mondino T. Three-dimensional static analysis of magneto-electro-elastic composite shells. Compos Struct 2025;374:119725.
56. Hildebrand FB, Reissner E, Thomas GB. Technical note number 1833 - notes on the foundations of the theory of small displacements of orthotropic shells. Washington (USA): NACA - National Advisory Committee for Aeronautics; 1949.
57. Povstenko Y. Fractional thermoelasticity. Switzerland: Springer International Publishing; 2015.
58. Brischetto S, Torre R. Convergence investigation for the exponential matrix and mathematical layers in the static analysis of multilayered composite structures. J Compos Sci 2017;1:19.
59. Kulikov GM, Plotnikova SV. Exact 3D thermoelectroelastic analysis of piezoelectric plates through a sampling surfaces method. Mech Adv Mater Struct 2015;22:33–43.
60. Tornabene F. Hygro-thermo-magneto-electro-elastic theory of anisotropic doubly-curved shells. Bologna (Italy): Società Editrice Esculapio; 2023.
61. Pan E. Three-dimensional Green's functions in anisotropic magneto-electro-elastic bimaterials. Z Angew Math Phys 2002;53:815–38.